Aggregation of *recount3* RNA-seq data improves inference of consensus and tissue-specific gene co-expression networks

Prashanthi Ravichandran[1], Princy Parsana[2], Rebecca Keener[1], Kaspar D. Hansen[1,3,4], Alexis Battle[*,2,4,5,6]

1. Department of Biomedical Engineering, Johns Hopkins University, Baltimore, MD, USA
2. Department of Computer Science, Johns Hopkins University, Baltimore, MD, USA
3. Department of Biostatistics, Johns Hopkins School of Public Health, Baltimore, MD, USA
4. Department of Genetic Medicine, Johns Hopkins University, Baltimore, MD, USA
5. Malone Center for Engineering in Healthcare, Johns Hopkins University, Baltimore, MD, USA
6. Data Science and AI Institute, Johns Hopkins University, Baltimore, MD, USA

* Corresponding author

Alexis Battle, PhD
ajbattle@jhu.edu

Keywords

Gene co-expression networks (GCNs), Graphical lasso, *recount3*, Public RNA-seq data, SRA, GTEx, TCGA, Data aggregation, Context-specificity, Complex trait heritability, s-LDSC.

Abstract

Background

Gene co-expression networks (GCNs) describe relationships among expressed genes key to maintaining cellular identity and homeostasis. However, the small sample size of typical RNA-seq experiments which is several orders of magnitude fewer than the number of genes is too low to infer GCNs reliably. *recount3*, a publicly available dataset comprised of 316,443 uniformly processed human RNA-seq samples, provides an opportunity to improve power for accurate network reconstruction and obtain biological insight from the resulting networks.

Results

We compared alternate aggregation strategies to identify an optimal workflow for GCN inference by data aggregation and inferred three consensus networks: a universal network, a non-cancer network, and a cancer network in addition to 27 tissue context-specific networks. Central network genes from our consensus networks were enriched for evolutionarily constrained genes and ubiquitous biological pathways, whereas central context-specific network genes included tissue-specific transcription factors and factorization based on the hubs led to clustering of related tissue contexts. We discovered that annotations corresponding to context-specific networks inferred from aggregated data were enriched for trait heritability beyond known functional genomic annotations and were significantly more enriched when we aggregated over a larger number of samples.

Conclusion

This study outlines best practices for network GCN inference and evaluation by data aggregation. We recommend estimating and regressing confounders in each data set before aggregation and prioritizing large sample size studies for GCN reconstruction. Increased statistical power in inferring context-specific networks enabled the derivation of variant annotations that were enriched for concordant trait heritability independent of functional genomic annotations that are context-agnostic. While we observed strictly increasing held-out log-likelihood with data aggregation, we noted diminishing marginal improvements. Future

directions aimed at alternate methods for estimating confounders and integrating orthogonal information from modalities such as Hi-C and ChIP-seq can further improve GCN inference.

Background

Critical cellular processes including the maintenance of cellular identity, homeostasis, and the cellular response to external stimuli are orchestrated through complex transcriptional co-regulation of multiple genes [1–4]. Gene Co-expression Networks (GCNs) are a commonly used framework to describe gene-gene relationships and are comprised of nodes that represent genes and edges linking co-expressed genes [5]. A comprehensive catalogue of gene co-expression relationships has the potential to characterize genes with unknown functions [6], identify regulatory genes [7], determine changes in regulatory mechanisms that are key to cellular identity [8], and prioritize genes that drive phenotypic variability [9]. Despite the utility of gene networks in understanding biological systems, network inference is still a challenging problem and suffers from both false positive and negative edges [10]. In particular, the typical sample size of most RNA-seq studies is orders of magnitude smaller than the number of gene pairs over which regulatory relationships are inferred, making network inference an underdetermined problem. Additionally, factors such as the stochastic nature of gene expression, experimental noise, missing data, and unobserved technical confounders make it difficult to avoid false positives or negatives. Since the number of possible gene-gene interactions scales with the square of the number of genes examined, a potential solution to increase statistical power by reducing network complexity has been to infer modules or groups of co-expressed genes that are regulated by one or more transcription factors rather than individual gene interactions [11]. While this approach has been successful at decreasing the number of hypotheses tested, and thereby increasing statistical power [12], it does not identify detailed network structure or distinguish between direct and indirect gene interactions. In contrast, network inference by graphical lasso [13, 14] results in the identification of pairwise edges reflecting direct effects, such that the absence of an edge implies the conditional independence of the genes when all other genes are observed. Further, the formulation of graphical lasso enables flexible penalization based on network density which aids in the identification of a network structure that improves the discovery of true gene-gene interactions while reducing false positives [15]. Here, we focus on improving the statistical power of network inference by significantly increasing the number of samples used in network inference, leveraging large-scale publicly available and uniformly processed RNA-seq data from *recount3* [16] which includes human RNA-seq samples from GTEx [17], TCGA [18], and SRA [19, 20].

Since the *recount3* project consists of RNA-seq data compiled from diverse data sources and multiple tissues with inconsistent sample characteristics, we developed a data pre-processing pipeline to identify and exclude outliers, harmonize the observed gene expression, and cluster samples into meaningful biological contexts such that we can reliably infer GCNs. We utilized 95,280 samples following quality control and pre-processing to infer three consensus networks: a universal network, a cancer network, and a non-cancer network, in addition to 27 context-specific networks which included 7 novel contexts only found in *recount3*. We compared strategies for confounder adjustment and data aggregation and found that accounting for confounders in each study followed by the weighted aggregation of covariance matrices by prioritizing studies with more samples resulted in networks with better generalizability and increased ability to recapitulate known biological gene-gene relationships. We observed that context-specific networks constructed using a combination of SRA and GTEx samples outperformed tissue-specific networks inferred solely using GTEx samples at recapitulating known tissue-specific protein-protein interactions (PPIs) and assigning tissue-specific transcription factors to central nodes, demonstrating the value of data aggregation in GCN inference. Furthermore, using S-LDSC [21] we observed that our context-specific networks had significant heritability enrichment attributed to network features when examining traits related to the tissue context. In conclusion, our work provides a carefully annotated RNA-seq data set, outlines best practices for GCN inference by leveraging publicly available RNA-seq data, and a set of consensus and context-specific networks that will aid the scientific community in achieving the full potential of GCN inference in biomedical research.

Results

A. Manual annotation and clustering of RNA-seq data from *recount3* identified 27 unique biological contexts

We downloaded uniformly processed RNA-seq samples from humans using the *recount3* R package [16] comprised of experiments from three data sources, The Sequence Read Archive (SRA) [19, 20], Genotype-tissue Expression (GTEx version 8) [17], and The Cancer Genome Atlas (TCGA) [18] and selected 1,747 projects that included 30 or more samples each. Following quality control **(Methods)**, 95,280 human bulk-RNA sequencing samples remained from 50 GTEx tissues (18,828 samples), 33 TCGA cancer types (11,091 samples), and 884 SRA studies (65,361 samples) **(Fig. 1 A)**. The aggregated data includes samples from a wide array of tissues, cell types, and diseases. While GTEx and TCGA studies included metadata specifying the tissue of origin and disease status for all samples, SRA studies had inconsistent nomenclature. Therefore, to obtain reliable labels for SRA samples, we manually parsed sample descriptions to obtain sample characteristics corresponding to tissue type and disease status for 65,361 SRA samples **(Methods)**. Based on curated annotations, 93.5% of TCGA samples and 30.4% of SRA samples were cancer. In contrast, all GTEx samples were non-cancer, as expected **(Fig. 1 B)**. Tissue labels with the greatest number of samples across all three data sources included blood, central nervous system, breast, skin, and lung **(Fig. 1 C)**. SRA included 224 distinct tissue labels derived from manual annotation that was not observed in GTEx or TCGA, and reflected a wide range of disease states including Type I Diabetes, Alzheimer's disease, bipolar disorder, arthritis, cancer, and infectious conditions **(Fig. 1 D)**. We grouped SRA samples based on their study accession IDs, GTEx samples by tissue, and TCGA samples by cancer code (**Methods**). To simplify terminology, we defined each group of samples from a data source as a single study. To leverage the extensive biological diversity in the data, we inferred two broad types of networks: consensus and tissue context-specific (context-specific). Our universal consensus network included all samples, regardless of tissue or disease. Our non-cancer consensus network included healthy samples and samples with disease status other than cancer. Finally, our cancer consensus network solely included cancerous samples. We restricted our context-specific networks to non-cancerous samples grouped by tissue context. We did not examine differential coregulation resulting from non-cancer disease, and regressed these effects from gene expression. Thus, by including SRA, *recount3* provides an unprecedented opportunity to examine unique contexts that were not previously studied in GTEx and TCGA.

Across the three data sources, SRA, GTEx, and TCGA, we obtained 266 unique manually annotated tissue labels with a median sample size of 31 which was much lower than the number of protein-coding genes. Therefore, we used a study-pooling strategy based on related tissue context to increase power **(Methods)**. Mapping manual annotations to tissue contexts **(Additional File 1: Supp. Table I)** generated 48 tissue contexts across 63,193 non-cancerous samples for context-specific network analysis. In each context, to ensure that a tissue context represented samples with similar cell-type composition as estimated by xCell [22] deconvolution, we learned a joint lower-dimensional t-SNE embedding using cell-type deconvolution scores, and for 25 contexts with more than 500 samples before outlier exclusion, we detected and excluded outliers **(Additional File 2: Supp. Fig 1)**. For the immune context, we observed that samples displayed extensive heterogeneity in cell-type composition. Thus we further separated this group into B cells, PBMCs/ T cells, and myeloid cells **(Additional File 2: Supp. Fig 2)**.

In total, we obtained 27 contexts including 7 tissue contexts that were not present in GTEx including airway, eye, human embryonic stem cells, induced pluripotent stem cells, multipotent cells, myeloid cells, and PBMCs / T cells **(Fig. 1 E)**. The number of samples present in each tissue context following outlier exclusion varied from 8,797 (Blood) to 485 (Multipotent cells) **(Fig. 1 F).** Further, for tissues that were present in GTEx, the ratio of the number of samples across all data sets to those in GTEx only ranged from 14.13 (Kidney) to 1.01 (Esophagus) **(Fig. 1 F)**. These harmonized samples have increased context resolution, i.e. include novel contexts which were not examined in GTEx, and increased sample size which can be used to improve the inference of consensus and context-specific networks.

B. Data aggregation improves the inference of consensus and context-specific GCNs

The median study-specific sample size across the three data sources was 44 for SRA, 309 for TCGA, and 285 for GTEx. Further, 766 of 884 SRA studies had a sample size lesser than 100. PC-based data correction has been used within a single study to reduce potential false positive gene regulatory associations [23, 24], but best practices for applying PC-based data correction in the context of aggregating multiple studies to infer GCNs have not been fully examined. First, we sought to determine whether data correction should be performed jointly across all samples, across samples belonging to a specific tissue context and multiple studies, or across samples from a specific tissue context and a specific study. We observed that PCs recapitulate different sample characteristics depending on the level at which data aggregation is performed. PCs calculated across all samples were driven predominantly by tissue labels followed by technical confounders (e.g. study and data source) **(Additional File 2: Supp. Fig 4 A-D, Supp. Fig 5 A)**. PCs which were calculated across samples belonging to a single tissue context (blood) but multiple studies were predominantly driven by study and data source. Further, accounting for tissue heterogeneity enabled us to better model cancer status and disease annotations using PCs **(Additional File 2: Supp. Fig 4 E-H, Supp. Fig 5 B)**. Finally, when we limited samples to a specific tissue context and a specific study (GTEx-skeletal muscle), we found that the top PCs were significantly associated with technical batch, consistent with the findings of Parsana et al. [24] **(Additional File 2: Supp. Fig 4 I-L, Supp. Fig 5 C)**. Thus regressing PCs computed by accounting for tissue and cross-study heterogeneity from expression is integral to excluding technical effects and unwanted biological signals.

In addition to comparing the effect of PC-based data correction, before and post-aggregation, where the number of PCs is selected based on the permutation method described by Buja et. al [25] and Leek et. al [23], we sought to examine the consequences of aggregating empirically estimated covariance matrices considering all studies equally (unweighted aggregation) as compared to weighting covariance matrices from studies with a greater number of samples more (weighted aggregation) on GCN inference. Thus, we used 4 paradigms: (1) Aggregating data before PC-based data correction followed by estimation of empirical covariance from residual expression, (2) PC-based data correction applied to individual studies followed by aggregation of residual expression and joint estimation of empirical covariance, (3) Unweighted aggregation of covariance matrices inferred from each study separately after study-specific PC-based correction and (4) Weighted aggregation of covariance matrices computed from individual studies following study-specific PC-based data correction, where the weights were the ratio of the study sample size to the total number of samples used in network reconstruction **(Fig. 2 A, Methods)**.

To compare strategies, we split non-cancerous samples into two data splits, GTEx and SRA **(Additional File 2: Supp. Fig 6)**, followed by network inference by graphical lasso on one of the two data splits and evaluation with the held-out split by computing the held-out log-likelihood. Details pertaining to the number of studies, samples and median PCs regressed for incremental data aggregation are provided in **Additional File 3: Supp. Table II**. Additionally, we assessed the recapitulation of known biological pathways by computing the F1-score of finding canonical gene-gene relationships compiled from KEGG [26], Biocarta, and Pathway Interaction Database [27] obtained using Enrichr [28, 29] **(Additional File 4: Supp. Table III)**. Paradigms in which PC-based data correction preceded aggregation led to a strict increase in held-out log-likelihood and F1-scores of known gene relationships from canonical pathways with the addition of more studies **(Fig. 2 B, C, Additional File 2: Supp. Fig 7, 8)**. This suggests that data aggregation resulted in GCNs with greater generalizability and recapitulated known biology better when technical confounders were estimated and regressed for individual studies. Since data aggregation led to a decrease in the network density for a particular value of the penalization parameter **(Additional File 2: Supp. Fig 9)**, we tested whether estimating denser networks would result in higher held-out log-likelihood specifically when the networks were inferred over a greater number of samples, but instead observed that higher densities led to overfitting and lower generalizability **(Additional File 2: Supp. Fig 10)**. Further, the marginal improvement in network reconstruction diminished with the subsequent rounds of aggregation. While all methods that estimated technical confounders within each study performed similarly and were superior to estimating technical confounders across all samples when evaluated by held-out log-likelihood **(Fig 2 D)**, we found that weighted aggregation of covariance matrices led to a slight improvement in the F1-score of the networks when compared to canonical pathways **(Fig. 2 E)**, suggesting that this is the optimal strategy among the alternatives compared.

We inferred consensus GCNs across diverse tissues by weighted aggregation of covariance matrices estimated from residual expression and graphical lasso **(Methods)**. In addition to a universal consensus network which was inferred across 966 studies with sample size greater than or equal to 15, amounting to 95,276 samples across 48 tissue contexts, we constructed a non-cancer consensus network and a cancer consensus network. The non-cancer consensus network reflects data aggregated across 629 studies and 63,031 samples, and the cancer network reflects 386 studies and 29,967 samples **(Fig. 2 F)**. We evaluated each consensus network to recapitulate previously reported gene-gene interaction using the F1 score. Across a range of network densities, we obtained a higher estimate of the F1 score from the universal consensus network, followed by non-cancer and cancer consensus networks, which mirrors differences in sample size **(Fig. 2 G)**.

We inferred networks across 27 tissue contexts and examined the impact of data aggregation on context-specific network reconstruction by considering GTEx samples (GTEx only) or by aggregating across samples from all data sources for that tissue context. The number of samples, studies, and median study-specific sample size for each tissue context in either aggregation setting are provided in **Additional File 2: Supp. Fig 3**. As in the consensus network inference, we used weighted aggregation of covariance matrices as the input to network inference by graphical lasso (**Methods**). To quantify the improvement in network reconstruction with data aggregation, we examined two tissue contexts with the largest sample size: blood and central nervous system (CNS). In both cases, we sequentially aggregated the blood or CNS SRA studies and computed the held-out log-likelihood utilizing context-matched GTEx samples. Similar to the results obtained from our consensus network analyses, we found that data aggregation led to a strict increase in held-out log-likelihood with additional studies and the greatest increase was observed while aggregating the first 20 studies (blood) and 15 studies (CNS) **(Methods, Fig. 2 H, I)**.

Orthogonally, we verified that our networks recapitulated known context-specific gene relationships by examining the enrichment of previously known tissue-specific protein-protein interactions (PPIs) from SNAP [30] in edges belonging to six tissue context-specific networks (adipose, blood, CNS, liver, lung, and skin) **(Methods)**. Data aggregation and increased sample size in the network significantly increased the estimated odds ratio of tissue-specific PPIs in the liver (Median GTEx OR = 7.85, Median Aggregate OR = 38.85, p = 0.03) and skin (Median GTEx OR = 21.83, Median Aggregated OR = 27.09, p = 0.05), and there was weak enrichment in adipose (Median GTEx OR = 18.49, Median Aggregated OR = 21.14, p = 0.06). In other tissue contexts, we observed a higher median odds ratio of PPI enrichment in networks inferred by data aggregation compared to GTEx-only networks **(Fig. 2 J)**. Thus, we demonstrated that data aggregation led to the improved inference of consensus networks that capture ubiquitous biological pathways and tissue context-specific networks that capture tissue biology by observing better network generalizability and reproduction of known biological processes.

C. Central network nodes are evolutionarily constrained and include genes that are critical to tissue identity

The biological information captured by a GCN can be evaluated by comparing individual network edges, by examining whether there are edges between genes that are known to interact in a particular cellular pathway [31], or by examining the properties of hubs [32–34], network nodes with a high number of connections. Since eukaryotic transcriptional networks typically consist of a subset of genes, often transcription factors, that regulate many downstream target genes [35], we chose specific network densities such that the selected networks are approximately scale-free **(Methods, Additional File 2: Supp. Fig 11; Additional File 5: Supp. Table IV, Additional File 6: Supp. Table V)**. We computed different measures of centrality corresponding to each network node and tested for the enrichment of genes involved in GO terms that reflect ubiquitous or context-specific processes **(Additional File 7: Supp. Table VI)** among network nodes selected with progressively increasing thresholds for degree centrality against a background of all 18,882 protein-coding genes **(Methods)**. Central nodes from all three consensus networks were strongly enriched for genes involved in functions such as microtubule-based process, chromosome organization, and regulation of organelle organization **(Fig. 3 A, Additional File 2: Supp. Fig 12)**. In contrast, we found that central nodes from blood context-specific networks were enriched for genes associated with platelet activation, leukocyte differentiation, and leukocyte chemotaxis to a greater extent than central genes derived from either consensus or a discordant context-specific network (CNS) **(Fig. 3 B)**. Further, these trends were reflected across multiple tissue contexts; context-specific networks corresponding to CNS **(Fig. 3 C)**, skin, liver, and lung were enriched for genes associated with tissue-matched GO terms **(Additional File 2: Supp. Fig 13)**. Thus, while central genes from consensus networks included genes involved in essential cellular processes, context-specific gene relationships are lost with global aggregation and are unlikely to be recovered by increasing the sample size.

Next, we evaluated whether hub genes were evolutionarily constrained and their role in complex traits or diseases **(Methods)**. We first binned network nodes such that genes with no neighbors were assigned to Quintile 1, and those with at least 1 connecting edge were grouped based on estimated quantiles of closeness centrality. Consensus network hub genes (Quintile 5) had a significantly higher excess overlap (>1) with evolutionarily constrained gene sets than peripheral nodes (Quintiles 1-3), using metrics including high pLI genes, high s_{het} genes, and high missense Z-score genes. These trends were similar in context-specific networks with some variation in the strength of the trend across tissues likely driven by sample size differences and differential power in inferring these networks **(Fig. 3 D, Additional File 2: Supp. Fig 15)**. We then examined the enrichment of eQTL-deficient, ClinVar, OMIM, and FDA drug-targeted genes across quintiles of network centrality **(Additional File 2: Supp. Fig 14, 15, Additional File 8: Supp. Table VII)**. We observed that peripheral genes (Quintile 1) and central genes (Quintile 5) of consensus networks exhibited an excess overlap > 1 of eQTL deficient genes (those which lacked significant *cis*-regulatory variants), while genes with intermediate connectivity were depleted of eQTL deficient genes, while the six context-specific networks had widely variable trends. While central genes from consensus networks were weakly depleted for OMIM and FDA drug-targeted genes, we observed an excess overlap > 1 of hub genes belonging to context-specific networks. This could be explained by our earlier observations that central nodes from consensus networks were involved in essential and non-specific cellular processes while central nodes from context-specific networks were both specific and critical to tissue identity, thus, altering central consensus network hub nodes may have widespread and potentially deleterious off-target effects while context-specific hub nodes may identify targetable genes with tissue-specific effects. Finally, we observed that matched tissue-specific transcription factors (TFs) from Pierson et. al [36] **(Additional File 9: Supp. Table VIII)** had a significantly greater number of neighbors than 88 general TFs for context-specific networks corresponding to blood ($p < 1e-4$), lung ($p < 1e-4$), and skin ($p < 0.01$), while in other tissues, except for CNS, the median degree of tissue-specific TFs was greater than general TFs and non-transcription factors **(Methods)**. In contrast, while tissue-specific and general TFs had more neighbors in consensus networks when compared to non-transcription factors, we found no significant differences in the degree distribution of tissue-specific TFs to general TFs in either the universal or non-cancer consensus network **(Fig. 3 E)**. Therefore, while both consensus and context-specific central genes were enriched for genes under high-selection pressure, context-specific hub nodes were more likely to be OMIM genes, drug targets and tissue-specific TFs.

We examined similarities and differences between network architectures of the non-cancer consensus and cancer consensus networks based on shared and distinct hub genes, since central genes are likely to be more relevant to network functionality [32], and the identification of hubs has led to the discovery of genes involved in cancer [33, 34], tissue regeneration [37], and other diseases [38, 39]. Specifically, we found 296 shared hubs between cancer ($\lambda = 0.24$, 7552 edges) and non-cancer ($\lambda = 0.18$, 7,355 edges) consensus networks, and 312 hubs which were specific to the cancer consensus network **(Additional File 10: Supp. Table IX)**. Cancer-specific hub genes were enriched for pathways such as ncRNA metabolic processing (GO:0034660, $p = 5.2e-02$) which is believed to play a role in metabolic reprogramming in cancer, DNA damage response

(GO:0006974, p = 1.17e-12) which has been posited to play a role in cancer cell survival in non-optimal conditions, and response to ionizing radiation (GO:0010212, p = 6.1e-04). Further, we found that cancer-specific hub genes were enriched for a plethora of DNA repair and replication pathways including, double-strand break repair via homologous recombination (GO:0000724, p = 6.36e-06), recombinational repair (GO:0000725, p = 1.35e-06), interstrand cross-link repair (GO:0036297, p = 5.48e-03), and double-strand break repair via break-induced replication (GO:0000727, p = 1.36e-03) **(Additional File 11: Supplementary File 1)**.

To examine whether network properties were shared between related tissues we compared the overlap of hub, we considered all hub genes found in at least two tissue contexts (N=1,956). Grouping tissue contexts based on hub genes using non-negative matrix factorization with eight latent factors **(Methods)** led to the grouping of related tissues such as blood and PBMCs/T cells (Factor 7) **(Fig. 3 F, Additional File 12: Supp. Table X)**. As expected, we found that hub genes that led to the grouping of blood and PBMCs/T cells were enriched for defense response (GO:0006952, p = 2.7-24) and cytokine production (GO:0001816, p = 9.9e-07) **(Additional File 13: Supplementary File 2)**. Further, Factor 6 which led to the grouping of hESCs, iPSCs, and multipotent cells comprised of hub genes which were enriched for gastrulation (GO:0007369, p = 5.9e-04) and circulatory system development (GO:0072359, p = 6.2e-03) **(Additional File 14: Supplementary File 3)**.

D. Genes with high network centrality are proximal to variants enriched for complex trait heritability

Previous work by Kim et al. [40] reported that network topology annotations did not contribute to heritability once the LDSC baseline model [21] was included. We examined whether data aggregation would increase the utility of network features for heritability analysis independently of baseline functional annotations. We meta-analyzed estimates of heritability enrichment, the ratio of the proportion of heritability explained by SNPs belonging to an annotation to the proportion of SNPs in the annotation, and τ^*, an estimate of the heritability of SNPs unique to the annotation [21], using a random effects model to obtain a summary of effect sizes estimated for a set of 42 independent traits considered by Kim et al. **(Methods, Additional File 15: Supp. Table XI)**. We estimated both heritability enrichment and τ^* by either conditioning an annotation corresponding to whether a variant was located in a 100 kilobase window of all protein-coding genes (all-genes annotation), or conditioning on 97 functional annotations such as known enhancer and promoter regions which are included in the baseline-LD model and the all-genes annotation (all-genes + baseline). Similar to the results found by Kim et al., we observed a significant estimate τ^* corresponding to our consensus network-derived annotations when conditioning on just the all-genes annotation, however, when conditioning on the baseline-LD model, the τ^* observed for consensus network-derived annotations were no longer significant **(Fig. 4 A)**. While we found no significant differences in enrichment across network density when conditioned on the all-genes annotation, we observed that τ^* decreased with a decrease in network density.

There were no significant differences in either enrichment or τ^* with network density when conditioning on the baseline-LD annotations **(Additional File 2: Supp. Fig 16)**. Further, our observations were not dependent on the traits studied and remained consistent when we applied s-LDSC to 219 UKBB traits **(Additional File 16: Supp. Table XII; Additional File 2: Supp. Fig 17)**

A possible explanation for the lack of heritability enrichment signal unique to network annotations is the redundancy between the baseline LD annotations and network topology annotations. Therefore, we hypothesized that context-specific data aggregation could prioritize variants enriched for heritability of concordant traits independent of baseline annotations. We applied s-LDSC to network centrality annotations derived from networks inferred only from GTEx blood samples (blood GTEx), networks inferred by aggregating *recount3* blood samples (blood), and as a control, networks inferred by aggregating all samples (universal consensus), for a subset of 9 blood-related traits from the 42 independent traits (Crohn's disease, rheumatoid arthritis, ulcerative colitis, eosinophil count, platelet count, red blood cell count, red blood cell width, white blood cell count, and eczema) **(Additional File 17: Supp. Table XIII)**. As with the consensus networks, tissue-specific networks displayed similar trends in heritability estimates with network density **(Additional File 2: Supp Fig 18, 19)**. When we conditioned on the baseline-LD annotations, we observed that annotations derived from the blood consensus networks had a significant τ^* across all centrality annotations, while blood GTEx networks had a significant τ^* for strength, degree, maximum weight and page rank **(Fig. 4 B)**. In contrast, we did not observe a significant τ^* corresponding to annotations derived from the universal consensus network. We examined the generalizability of our results by conducting a similar experiment in CNS samples, another tissue with a large sample size. We applied s-LDSC to annotations derived from CNS networks inferred from GTEx samples (CNS GTEx), CNS networks inferred by aggregating samples from *recount3* (CNS consensus), and the universal consensus networks for CNS-related traits which included waist-hip ratio adjusted BMI from the earlier set of 42 traits, as well as 7 traits from the Psychiatric Genomics Consortium (Alzheimer's, epilepsy, Parkinson's, bipolar disorder, smoking cessation, schizophrenia, major depressive disorder, and number of alcoholic drinks per week) **(Additional File 18: Supp. Table XIV)**. We found that annotations derived from both universal consensus and CNS-specific networks led to significant non-zero τ^* when conditioning on the baseline-LD model. While we note that significant non-zero τ^* was observed for the consensus networks for the chosen set of CNS traits in contrast to the 42 independent traits, possibly due to power, study quality, and other attributes of the GWAS, we found that annotations from tissue-specific networks led to significantly higher estimates of τ^* and outperformed consensus networks **(Fig. 4 C)** for all centrality measures except closeness. Further, for betweenness, maximum weight, and page rank centrality, CNS consensus networks outperformed CNS GTEx networks, similar to the results in blood, demonstrating context-specific data aggregation results in network annotations that are enriched for trait heritability across tissue contexts. Across both sets of blood- and CNS-related traits, we found that page rank centrality-derived annotations, which captured both the number of connections that a node has in addition to the centrality of its neighbors to determine the importance of a connection, performed consistently well. We conclude that context-specific aggregation results in identifying network central genes that are enriched for the heritability of concordant traits, and an increased sample size leads to a greater heritability enrichment signal.

Discussion

GCNs aid in determining changes in regulatory mechanisms that are key to cellular identity and prioritizing genes that drive phenotypic variability. However, conventional network analyses are often too underpowered to reliably discover gene-gene relationships and are compromised by spurious false positives and false negatives that result from limited power, noise, and unobserved technical confounders. We leveraged publicly available RNA-seq data from *recount3* and manually curated tissue/cell type annotations to improve the inference of consensus and context-specific GCNs. Utilizing data splits, we demonstrated that accounting for confounders within individual studies followed by weighted aggregation of empirical covariance matrices led to the best improvement in network characteristics with data aggregation across multiple paradigms.

We then inferred three consensus networks (universal, non-cancer, and cancer networks) that recapitulated ubiquitous biological processes. Further, we aggregated data belonging to individual tissue contexts to infer 27 tissue context-specific networks that were enriched for matched tissue-specific PPIs and shared similarities across related tissues. All networks and sample annotations are made publicly available as a resource for future studies.

Central genes from both consensus and context-specific networks were enriched for high PLI, and high Phi genes, indicating that hub genes are enriched for genes under high selective pressure. Context-specific hub genes were enriched for FDA-approved drug targets and OMIM genes while central genes from consensus networks which were inferred over a greater number of samples were depleted for both categories. Thus, context-specific information was lost by global aggregation, cannot be recovered by data aggregation or increased sample sizes, and is important to identifying drug targets and disease mechanisms. While network central genes determined by global data aggregation in the consensus network did not explain trait heritability independent of known functional annotations in the baseline-LD model, we found that context-specific data aggregation prioritized variants enriched for concordant trait heritability that did not overlap with previously known functional annotations. Thus topological properties of genes from context-specific GCNs hold significant promise as a functional annotation for identifying genetic variation that contributes to complex trait heritability.

A commonly used approach to identify genes associated with complex traits is to use colocalization analysis between GWAS and eQTL studies, however, often only about half of the signals colocalize with an eQTL [41]. Recent work by Mostafavi et al [41] demonstrated that genes driving GWAS signals were often genes with complex context-dependent regulatory architecture and were depleted for eQTL variants. This has raised a call in the computational genomics community for orthogonal approaches to identify genes involved in complex traits. We found that annotations derived from context-specific GCNs are informative of trait heritability independent of context-agnostic functional annotations. This suggests that tissue- and context-specific network centrality and other network properties could be used to help prioritize genes near GWAS loci [42] or supplement eQTL data.

One of the major challenges in network inference remains the presence of unobserved technical confounders and undesirable biological signals which leads to spurious network edges and precludes causality claims. While PC-based data correction has been extensively utilized to reduce false positives resulting from confounding, recent work by Cote et. al [43] suggests that PC-based data correction, and related methods such as PEER [44] and CONFETI [45], may over-correct expression data and remove biological co-expression of potential interest. Correcting or modeling confounders is essential to network accuracy, so tuning parameters such as the number of latent factors to correct as well as exploring alternative methods will continue to be important. Alternate approaches to handle confounding and infer causal regulatory relationships include instrumental variable analysis through the construction of local genetic instruments as outlined by Lujik et al. [46], however, since central network nodes are evolutionarily constrained and tightly regulated, it can be challenging to construct well-tracking genetic instruments for central genes,. Publicly available RNA-seq data including *recount3*, the extensive annotations we provide, and recent work which illustrated genotype calling using RNA-seq data [47] could improve our ability to detect context-specific cis-regulatory effects, the reconstruction of local genetic instruments, and hence causal regulatory network inference.

Future directions aimed at improving GCN inference could leverage our extensively annotated sample characteristics and data aggregation strategies with complementary strategies including sharing information between related contexts [48] to increase the effective sample size, introducing constraints or priors corresponding to known regulatory relationships [49], and using alternate statistical measures of expression similarity that capture non-linear associations between genes [50]. Additionally, heuristic algorithms such as the one proposed by Opgen-Rhein et al. [51]

could be utilized to enrich our current networks with directionality information. Finally, while we studied tissue-contexts, we provide annotations of disease status which can be utilized to infer disease-specific GCNs.

Our finding that marginal improvement in network reconstruction decreases with continued data aggregation suggests that simply addressing statistical considerations due to sample size may have limitations for improving GCNs. Including orthogonal sources of information such as gene-enhancer associations inferred from Hi-C data [52] and transcription factor binding sites from ChIP-seq data [53], in addition to gene expression quantified by RNA-seq in both bulk and single-cell studies, might result in a more accurate understanding of the shared regulatory architecture between genes. Additionally, experimental protocols such as Perturb-Seq [54], which quantifies the transcriptional changes mediated by genetic manipulations on genes, processes, and states, could provide a new avenue for network inference and suggest causal mechanisms and edge directionality.

Conclusions

We demonstrated that data aggregation improved the inference of consensus and context-specific networks, particularly when properly accounting for latent confounding and between-study variability. While consensus networks prioritized ubiquitous biological processes, context-specific networks captured tissue-specific gene interactions. Further, context-specific networks prioritized variants that are enriched for trait heritability independent of overlap with baseline functional genomic categories suggesting that improving the detection of context-specific gene-gene interactions can shed light on the mechanisms that relate genetic variants to traits. Thus, meaningful data aggregation improves GCN inference and identifies how genes interact to produce complex phenotypes.

Methods

A. Data pre-processing and quality control

We downloaded uniformly processed RNA-seq samples from humans using the *recount3* R package [16] and selected 1747 projects that included 30 or more samples each **(Fig. 1A)**. Before normalization, we excluded samples with zero expression across all genes and genes that had zero expression across all samples in a project. We used in-built functions from the *recount3* package to compute the RPKM transformed count matrix, selected genes that were protein-coding, autosomal, and unambiguously mapped to the reference genome [55, 56], and generated the $log_2(RPKM + 1)$ count matrix for each project. Following preliminary processing, we applied a unique data processing pipeline based on the study of origin to exclude samples from micro-RNA and scRNA-seq experiments and summarized replicates. For projects belonging to GTEx, we excluded duplicates (which are labeled as STUDY_NA in the project attribute), as well as samples derived from the chronic myelogenous leukemia (CML) cell line and grouped samples by the tissue of origin to obtain 50 groups and 18828 samples.

Before identifying replicates, we excluded 67 TCGA samples that did not have sample type specified, followed by 39 samples which did not have patient ID present. We then identified replicates in the remaining TCGA samples as those samples that agreed on both patient ID as well as sample type and aggregated by computing the median across all replicates. We then grouped samples by their respective cancer code to obtain 33 groups and 11091 samples.

Finally, for projects from SRA, we began by excluding samples obtained by size fractionation. We then identified replicates, as those samples with an identical experiment accession number and aggregated across replicates by computing the median gene expression, this results in 200499 samples. To exclude microRNA projects that have erroneously been labeled bulk-RNA sequencing experiments, for each sample, we computed the fraction of genes with zero expression and excluded 89,101 samples where this fraction is greater than 50%. The *recount3* database includes manually curated tissue types and experiment types for 30473 samples of 373 SRA studies. The experiment types found included 4 categories, bulk RNA-sequencing, single-cell RNA-seq, small/micro RNA-seq and others. Based on the differences in the sparsity patterns of bulk RNA sequencing and other sequencing modalities, the authors developed a predictor to classify samples as either bulk or single-cell-based. We utilized these predicted labels to restrict our analysis to only bulk RNA-sequencing studies. Since predicted labels were not present for all samples, we excluded samples with keywords such as “single cell”, “scRNA”, “snRNA”, and “single nucleus” in the study abstract if it was found. Further, when the library selection information was available, we restricted our analysis to samples that contained either cDNA or RT-PCR in the library selection field. We also excluded studies which are known scRNA-seq experiments including, SRP096986, SRP135684, SRP166966, SRP200058, and SRP063998. For the remaining studies, we performed a text-based analysis to obtain the Study, Tissue, Organ, Biopsy, Cell, Disease, Source and Description from the metadata `sample_description` field. We then manually annotated 10179 unique combinations of these fields to obtain tissue, cancer status, and disease type. In this manner, we were able to obtain labels for 65361 samples which we grouped on the basis of the study accession IDs to form 884 SRA studies **(Additional File 19: Supplementary File 4)**. While we grouped GTEx samples by tissue of origin, SRA samples by study accession ID, and TCGA samples by cancer accession code, we refer to an individual group of samples as a “study” to simplify nomenclature. Further, we did not distinguish on the basis of disease state or cancer status while organizing the data, until we proceeded to compute the inputs to network inference.

B. Identifying tissue type and cancer status

Wilks et. al [16] demonstrated that for bulk RNA-seq data from humans, the largest source of variation in gene expression was correlated with tissue or cell type of origin, with the clear clustering of samples belonging to the same tissue extending to the top 4 principal components. We manually refined annotated labels and grouped samples by context using t-SNE dimensionality reduction and clustering 95484 samples and 5999 genes which had non-zero variance across all samples. Since it was not possible to differentiate cancerous and non-cancerous samples using differential clustering in the t-SNE space, we utilized manually annotated labels to restrict the analysis to non-cancerous samples.

Further, to facilitate the greatest possible increase in sample size, we combined similar tissues to form tissue categories **(Additional File 1: Supp. Table I)**. Since differences in gene expression across samples can be driven by factors other than the tissue of origin, such as experimental batch and library size, we obtained the relative enrichment of 64 distinct stromal and immune cell types by comparing the gene expression profile of an admixture sample from bulk tissue to curated gene expression signatures provided by `xCell [22]`. Once we computed the cell-type enrichment vectors for each sample, we performed t-SNE dimensionality reduction for visualization and clustering.

For 24 tissue categories that have more than 500 samples, we refined our sample selection by eliminating outliers using 6 different methods of outlier calling. These included

1. Z-score-based outlier calling: We computed the z-scores for each reduced dimension independently, samples which have a z-score greater than or equal to 3 in either dimension are labeled as outliers.
2. MAD-based outlier calling: For each dimension we computed the median absolute deviation as given by Eqn. 1

   $$MAD = Median(|X_i - \overline{X}|) \qquad \text{Eqn. 1}$$

   Where $\overline{X}$, is the mean of all observations. We computed the outlier score in each dimension using Eqn. 2

   $$S_{MAD} = |X_i - Median(X)| \,/\, MAD \qquad \text{Eqn. 2}$$

   We labelled a sample an outlier if S_{MAD} is greater than or equal to 3 in either dimension.
3. Tukey outlier calling: We computed the quartiles of each dimension and the $IQR = Q_3 - Q_1$. Samples which have a value lower than $Q_1 - 1.5 \times IQR$ or greater than $Q_3 + 1.5 \times IQR$ in either dimension are labeled outliers.

For each method below, we computed the Mahalanobis distance (MD) for each sample by estimating the covariance matrix C across all samples. The MD is given by Eqn. 3,

$$MD = (X_1 - X_2)^T . C^{-1} . (X_1 - X_2) \qquad \text{Eqn. 3}$$

To identify outliers, we used the additional criteria based on the MD outlined below,

4. Mahalanobis Z-score: Computed the z-scores across the MD metrics and labelled samples with a z-score greater than or equal to 3 as outliers.
5. Mahalanobis MAD: Computed the MAD-based outlier score on the MD using Eqn. 2, and labelled samples with a score greater than or equal to 3 as outliers.
6. Mahalanobis Tukey: Compute the quartiles of the MD estimates and the inter-quartile range (IQR). Label samples with an MD estimate lower than $Q_1 - 1.5 \times IQR$ or greater than $Q_3 + 1.5 \times IQR$ as outliers.

If a sample within a tissue category is labeled an outlier by at least 2 methods of outlier calling, then we excluded the sample for downstream network reconstruction. While this works with simpler tissue categories such as blood, skeletal muscle or colon where the samples have relatively homogenous cell type compositions, for the immune system, which comprises samples from the distinct myeloid, lymphoid and innate immune systems, these outlier metrics failed due to large intersample variation. Therefore for immune cell types, we first performed K-means clustering with 3 centroids. We annotated the three resulting clusters based on the representation of manually annotated labels in each cluster as either B-cells, myeloid cells (including monocytes and macrophages) and

PBMCs w/ T cells. For each cluster, we performed outlier detection using all six methods outlined above and excluded samples that were found to be outliers in any two methods.

C. Data correction and aggregation

Principal component (PC) based correction methods can account for technical and biological artifacts that confound gene expression measurements and reduce false positives in gene network inference [24]. However, these methods have been applied to one experiment and not across multiple experiments from disparate sources. We systematically compared 4 strategies of data aggregation including,

1. Aggregating data: Identify genes with non-zero expression and non-zero variance across all studies of interest, followed by aggregating the data, quantile normalization, scaling, and PC estimation. We determined the number of PCs to regress using the permutation method described by Buja et. al [25] and Leek et. al [23]. We then obtained the residuals by fitting a linear regression using the number of identified PCs. Finally, we quantile normalized the residuals and scaled each gene to have a mean of zero and unit variance and estimated the empirical covariance matrix.
2. Aggregating data adjusted for confounding: We considered each study individually, quantile normalized, scaled the data, and estimated PCs, followed by the determination of the optimal number of components to be regressed. We then obtained the residual gene expression using a linear model to regress latent variables corresponding to confounding. We aggregated across each individually corrected study by selecting genes that have non-zero expression and non-zero variance across all samples. Finally, we quantile normalized and scaled the

aggregated corrected gene expression and estimated the empirical covariance matrix.

3. Unweighted aggregation of covariance matrices: For each individual study, we quantile normalized and scaled the data, followed by PC-based data correction and computed residuals. To the residuals, we applied quantile normalization and scaling and estimated the empirical covariance matrix S_k for each study k. Assuming equal likelihood of error from each study we computed the unweighted average of covariance matrices $C_{unweighted}$ as described in Eqn. 4

$$C_{unweighted} = \frac{\sum_k S_k}{|K|} \qquad \text{Eqn. 4}$$

where $|K|$ is the total number of studies aggregated.

4. Weighted aggregation of covariance matrices: We repeated the process described previously in the computation of unweighted aggregation of covariance matrices to estimate study-level empirical covariance matrices S_k. We then assumed that studies with a larger sample size provide a better estimate of individual covariances and computed the weighted covariance as in Eqn. 5 and Eqn. 6

$$w_k = \frac{n_k}{\sum_k n_k} \qquad \text{Eqn. 5}$$

$$C_{weighted} = \sum_k w_k S_k \qquad \text{Eqn. 6}$$

D. Network reconstruction with graphical lasso

Following the computation of aggregate covariance matrices using the strategies outlined in the previous section, we infer gene regulatory relationships using graphical lasso [13]. The desired network structure is obtained by identifying the precision matrix, $\Theta = \Sigma^{-1}$ that maximizes the penalized log-likelihood given by Eqn. 7, where C is the estimated covariance matrix.

$$\widehat{\Theta} = argmin_{\theta} \; tr(C.\Theta) - log\,|\Theta| + \lambda||\Theta||_1 \qquad \text{Eqn. 7}$$

We estimated the precision matrix Θ across a range of λ between 0.04 to 1.00 in intervals of 0.02. For genes p and q, an edge connecting them exists if the corresponding entry in the precision matrix is non-zero as given by Eqn. 8

$$\widehat{N}_{p,q} = \begin{cases} 1, & if \; |\widehat{\Theta}_{p,q}| > 0 \\ 0, & otherwise \end{cases} \qquad \text{Eqn. 8}$$

E. Network evaluation to determine the optimal aggregation strategy

We applied all 4 methods of data aggregation to infer networks from non-cancerous samples using two data partitions - GTEx and SRA non-cancer. Since GTEx did not include any cancerous samples, we organized the samples by tissue-type and excluded any tissues with fewer than 15 samples, in this case, Kidney-Medulla. For the SRA non-cancer, we select samples which were annotated to be non-cancerous and organize them by the study accession IDs, we then exclude any studies which had fewer than 15 samples, resulting in 566 selected studies. For each data partition, we evaluated network improvement with sequential data aggregation as follows,

1. SRA non-cancer: An aggregate network inferred across 566 SRA studies from varying tissues that are non-cancerous. We order the studies by increasing sample size and aggregate 1, 100, 200, 300, 400, 500 and 566 studies to estimate empirical covariance matrices and infer networks using graphical lasso across λ ranging from 0.04 to 1.00.
2. GTEx non-cancer: An aggregate network inferred across 49 GTEx tissues and cell lines. We order tissues in increasing order of sample size and aggregate tissues in increments of 10 to obtain networks corresponding to 1, 10, 20, 30, 40 and 49 tissues across a range of λ between 0.04 and 1.00.

Details of the number of studies, samples, median sample size and principle components regressed are provided in **Additional File 3: Supp. Table II**. Following network inference, we evaluated the improvement in network inference as a function of sample size and method of data aggregation using two metrics, held-out log-likelihood and enrichment of known biological pathways. The metrics are computed as follows,

1. Held-out log-likelihood: For networks inferred using SRA data, the test set consisted of 6 GTEx tissues including Adipose Subcutaneous, Cells cultured fibroblasts, Heart left ventricle, Artery aorta, and Colon sigmoid. To evaluate networks inferred using GTEx samples we selected SRA studies with matched sample sizes including SRP116272, SRP151763, SRP150552, SRP174638, and

SRP187978. For each test study, we quantile normalized and scaled the data, followed by PC-based data correction and computed residuals. We then quantile normalized and scaled the residuals and computed the corresponding covariances matrices S_i for the i^{th} study. We computed the log-likelihood of the data observed in each held-out study as shown in Eqn. 9

$$L_i = n_i[log\,|\widehat{\Theta}| - tr(S_i \,.\, \Theta)] \qquad \text{Eqn. 9}$$

We then computed the average log-likelihood across all test data sets $i \in I$ as given by Eqn. 10 where $|I|$ is the total number of test data sets.

$$\overline{L} = \frac{\Sigma_i L_i}{|I|} \qquad \text{Eqn. 10}$$

2. Prediction of known biological pathways: We downloaded pathway information from KEGG, Biocarta and Pathway Interaction Database from Enrichr and selected those pathways that were annotated as canonical pathways by MSigDB. **Additional File 4: Supp. Table III** provides details on the number of gene sets from each source. Any pair of genes that have at least one pathway in common were assumed to have a true functional relationship. In total, we identified 9648013 such edges (U). For each inferred network $\widehat{N} = \{V, E\}$, where V is the set of genes over which we perform network reconstruction, and E is the set of edges between the gene pairs, we restricted the set of universal pathway edges to those between genes $G_1, G_2 \in V$. If S_{all} is the set of edges between all possible gene pairs such that $|S_{all}| = {}^{V}C_2$, then $U^C = S_{all} \setminus U$, and $E^C = S_{all} \setminus E$, we constructed the contingency table as follows,

a. True positives (TP) = $|U \cap E|$

b. False positives (FP) = $|U^C \cap E|$

c. True negatives (TN) = $|U^C \cap E^C|$

d. False negatives (FN) = $|U \cap E^C|$

We computed the precision, recall, and F1-score as described by Eqn. 11, Eqn. 12, Eqn. 13.

$$Precision = \frac{TP}{TP + FP} \qquad \text{Eqn. 11}$$

$$Recall = \frac{TP}{TP + FN} \qquad \text{Eqn. 12}$$

$$F1 - score = 2. \frac{Precision \times Recall}{Precision + Recall} \qquad \text{Eqn. 13}$$

F. Inference of consensus and tissue context-specific networks

We inferred consensus networks across samples from disparate tissues and cell types to capture shared biological pathways across contexts. Since weighted covariance aggregation yielded the best results across the 4 methods of data correction and aggregation, we first grouped SRA samples by the study accession ID, GTEx samples by the tissue of origin, and TCGA samples by the cancer code. To estimate the universal consensus network we did not exclude any samples. Thus, we aggregated 65361 samples from 884 SRA studies with a median sample size of 44, 11091 samples from 33 TCGA studies with a median sample size of 309, and 18824 GTEx samples from 49 tissues and a median sample size of 286. Prior to estimating non-cancer consensus networks, we first exclude all cancerous samples from each study, and only retain studies with 15 or more samples. Similarly, prior to estimating cancer consensus networks, we only include cancerous samples, and exclude studies with fewer than 15 samples. Since weighted covariance aggregation yielded the best results across the 4 methods of data correction and aggregation, we first etimated and adjusted for unknown technical confounders using Principal component analysis (PCA) in each group of samples. We computed the weighted empirical covariance matrix as detailed in Section II.c. We then inferred the network structure by optimizing penalized log-likelihood Eqn. 7 and thresholded the entries in the precision matrix as described by Eqn. 8 for a range of penalization parameters λ ranging from 0.08 - 1.00.

We inferred context-specific networks in 27 contexts with 500 or more samples. Details of the number of samples, studies, and median sample size across studies for each context are provided in **Additional File 2: Supp. Fig 13**. For 20 contexts including adipose, B cells, blood, breast, cardiac, central nervous system, colon, esophagus, fibroblasts, intestine, kidney, liver, lung, nervous system, pancreas, prostate, skeletal muscle, skin, stomach, and vascular we inferred networks either using GTEx sample only or by aggregating context-specific samples from recount3 which included GTEx. For each context-specific network, we first performed PC-based data correction within each study followed by covariance estimation and aggregation by weighting the covariance matrix with the proportion of study-specific sample size to the total number of samples as detailed in Eqn. 5 and Eqn. 6. We then inferred GCNs using graphical lasso using Eqn. 7 and Eqn. 8

G. Evaluating the impact of data aggregation on the inference of consensus and context-specific networks

To evaluate the improvement in the performance of consensus networks with data aggregation, we computed the precision, recall, and F1-score of observing known gene co-regulatory pairs compiled from KEGG, Biocarta and Pathway Interaction Database which were annotated as canonical pathways by MSigDB as detailed in **Methods (Section E)**. Specifically, we compared the F1-scores corresponding to the universal, non-cancer, and cancer consensus networks for network densities between 5000 and 500,000 edges.

In order to evaluate the impact of data aggregation on context-specific networks, we selected two contexts with the highest number of samples - blood and CNS. We obtained 64 SRA studies that were annotated to blood, and 40 SRA studies annotated to CNS. We sequentially aggregated SRA studies five at a time in each context in the increasing order of sample size and inferred GCNs using weighted aggregation of covariance matrices and graphical lasso as detailed in **Methods (Sections C, D)** over a range of penalization parameters λ varying from 0.10 to 1.00. For each data aggregation setting, we evaluated the network performance over a range of network densities by computing the held-out log-likelihood of GTEx samples belonging to the concordant tissue in a manner analogous to **Methods (Section E)**. Specifically, to evaluate the inferred blood networks, we utilized the empirical covariance matrix computed from 850 blood GTEx samples. Since GTEx contained 13 brain regions which were all annotated to the CNS context, we computed the held-out log likelihood corresponding to each brain region and computed the mean across regions to obtain a scalar measure of the network's generalizability.

Additionally, for 6 contexts, adipose, blood, CNS, liver, lung, and skin we compared networks inferred solely from GTEx samples to GCNs inferred from data aggregation based on the inclusion of known tissue-specific protein-protein interactions (PPIs). First, we selected networks that were inferred with the value of the penalization parameter between 0.12 and 0.50. We then downloaded tissue-specific PPIs present in PPT-Ohmnet_tissues-combined.edgelist.gz from SNAP which is compiled across 144 unique tissues [57–59]. We mapped the tissue labels present in SNAP to our contexts studied as given in **Additional File 20: Supp. Table XV**. After converting the protein identifiers using the R package `org.Hs.eg.db`, we performed Fisher's test to compute the odds ratio of finding tissue-specific PPIs in our context-specific networks when compared to a fully connected network as background. Specifically, we computed the following contingency matrix that we used as input to the R function `fisher.test()` where E is the set of edges present in our inferred network, P_t is the set of concordant tissue-specific PPIs, and E^c is the set of all edges absent in the network which is obtained by $U \setminus E$, where U is the set of all possible edges between the nodes, and $|U| = {}^{G}C_2$ where G is the set of genes over which we perform network inference.

	Edge present in tissue-specific PPIs	Edge absent in tissue-specific PPIs
Edge present in network	$\|P_t \cap E\|$	$\|E\| - \|P_t \cap E\|$

Edge not present in network	$\vert P_t \cap E^c \vert$	$\vert E^c \vert - \vert P_t \cap E^c \vert$

To compare between context-specific networks inferred solely from GTEx to those inferred across aggregated data, we performed the Wilcoxon rank-sum test to compare the odds ratios from each setting.

H. Sparsity parameter selection for consensus and context-specific networks

Previous analysis of gene regulatory networks indicates that eukaryotic [60] and prokaryotic transcriptional [61] networks exhibit an approximately scale-free degree distribution which concurs with the assumption that few transcription factors have the potential to regulate an multitude of target genes [35]. The power law degree distribution follows Eqn. 14 where $p(k)$ is the probability of a random node having k connections and γ is the power law scaling exponent.

$$p(k) = C \,.\, k^{-\gamma} \qquad \text{Eqn. 14}$$

Taking the logarithm, we get,

$$log\, p(k) = -\gamma\, log\, k + log\, C \qquad \text{Eqn. 15}$$

For each of the 3 consensus networks and 27 tissue-context specific networks, we used the R package `igraph` to estimate the degree distribution for each value of λ and the function `lm()` to estimate the slope $(-\gamma)$ and R^2. Finally, we computed the 95% confidence interval (CI) for the slope using the R function `confint()`. We then selected networks such that $2 \le LL(\gamma) \le UL(\gamma) \le 3$, and the $R^2 > 0.8$ where $LL(\gamma)$ and $UL(\gamma)$ correspond to the lower and upper limits of the 95% CI of γ. Details pertaining to the selected consensus networks and their corresponding values of the penalization parameter λ, network densities, regression slope and R^2 are provided in **Additional File 5: Supp. Table IV**. Similarly, the selected network densities, values of the regression slope and R^2 are provided for context-specific networks inferred from GTEx only and across all aggregated samples in 6 contexts which were used in downstream analysis is in **Additional File 6: Supp. Table V**.

I. Computing gene centrality measures based on network structure

Using measures of network connectivity, we computed centrality scores for each gene in the network. Given a weighted undirected graph G, first, we normalized the edge weights If E is the list of all edges in the network (excluding diagonals) and $E_{p,q}$ is the weight of an edge connecting genes p and q. Then the normalized weight $\widehat{E}_{p,q} = E_{p,q} / max(E_{i,j})$ for all $i, j \in Nodes(G)$ such that $i \neq j$. Using normalized edge weights we computed the following centrality scores for each gene p,

a. Betweeness(p): The betweeness centrality captures the number of shortest paths in a network that passes through the gene p. The shortest path between nodes $i, j \in Nodes(G)$ is the path where the sum of the edge weights is minimum.

b. Closeness(p): The closeness centrality captures the distance between a gene p to all other network nodes. We first obtained the weighted distance between gene p and gene i as given by Eqn. 18

$$d_{p,i} = \frac{1}{E_{p,i}} \qquad \text{Eqn. 18}$$

If the nodes p and i' are disconnected then we set $d_{p,i'}$ to 0. Finally, the closeness centrality of a gene p is given by Eqn. 19

$$C(p) = \frac{1}{\Sigma_{i \neq p} d_{p,i}} \qquad \text{Eqn. 19}$$

c. Degree(p): The degree of a gene p corresponds to the number of neighbors connected to p.

d. Maximum weight(p): The maximum weight of a node is the maximum weight of the edges that are connected to the gene p.

e. Page rank(p): The page rank of a node p is defined by Eqn. 20,

$$(1 - \alpha)/N + \alpha \sum_{u \in N(p)} Pagerank(u)/d^{+}(u) \qquad \text{Eqn. 20}$$

Where α is a damping factor, $N(v)$ are the in-neighbors of node p, and $d^{+}(u)$ is the out-degree of u. Because G is an undirected graph, pagerank treats it as a directed graph by making edges bi-directional. Specifically, in addition to the number of neighbors that a node p has, page rank incorporates information pertaining to the connectivity of the neighboring nodes.

f. Strength(p): The strength of a node is defined as the sum of the weights of all edges connected to the gene p.

J. Enrichment of specific pathways among central genes in consensus and context-specific networks

First we developed a general method to test for the enrichment of genes annotated to a specific GO term among network central genes. For a given network $N = \{V, E\}$

where V is the set of nodes and E the set of edges, we estimated the degree of each node as described in **Methods (Section I)** and estimated the maximum degree across all nodes. We then determined a series of degree thresholds, starting at 5 to the maximum degree in increments of 5. For a particular degree threshold, D_t we obtained all the network nodes with a degree $D_i \leq D_t$, which forms the test set of genes T, such that $T \subseteq V$. To determine the enrichment of genes associated with a particular GO term corresponding to a biological process (GoG), we first computed the following contingency matrix where G is the set of 19950 protein-coding genes where $T^c = G \backslash T$

	Gene present in GO term	Gene absent in GO term
Gene present in test set	$\lvert T \cap GoG \rvert$	$\lvert$T$\rvert$ - $\lvert T \cap GoG \rvert$
Gene absent in test set	$\lvert T^c \cap GoG \rvert$	$\lvert T^c \rvert - \lvert T^c \cap GoG \rvert$

We then performed Fisher's test with the alternative hypothesis that the odds ratio of finding GO related terms is greater in the test set T and estimated p-values.

To evaluate the universal, non-cancer and cancer consensus networks, we first selected the value of the penalization parameter such that the resulting network density was ~ 7000 edges. We then determined the odds ratio of finding genes belonging to ubiquitous biological processes among network nodes selected by successively increasing degree thresholds. Further, we computed the odds ratio of finding genes belonging to ubiquitous processes in blood and CNS networks inferred across all samples from *recount3* with ~ 7000 edges.

To evaluate a context-specific network such as blood, we first selected a blood network inferred solely from GTEx samples and a network inferred by data aggregation across all samples from *recount3* such that the resulting network density was ~7000, and the node degree distribution was scale-free. As negative controls, we included a different context-specific network inferred across aggregated samples, the universal and non-cancer consensus network. For blood, we specifically tested for the enrichment of processes such as leukocyte migration, leukocyte activation and blood coagulation. We repeated this analysis for 5 other context-specific networks - CNS, skin, lung, liver, and adipose by selecting related GO terms and determining the enrichment of functional genes among network central genes. A complete list of GO terms that were tested for each context is described in **Additional File 7: Supp. Table VI.**

K. Excess overlap of genes grouped by centrality measures in consensus with known evolutionarily constrained and functionally prioritized gene sets

We group genes for each consensus network such that the first bin includes genes with no edges (with a degree of zero), the second bin contains nodes with a degree in the lowest 25th percentile, the third bin includes nodes with a degree in the 25th - 50th percentile, the fourth bin includes genes with degree in the 50th - 75th percentile and the fifth and final bin includes genes with a degree greater than the 75th percentile. For genes in a given bin, we compute the excess overlap with known 9 evolutionarily constrained and functional gene sets used by S.Kim et al. which include,

1. High pLI genes [62]: 3,104 loss-of-function (LoF) genes with pLI > 0.9, i.e., strongly depleted for protein-truncating variants.
2. High S_{het} genes [63]: 2,853 constrained genes with $S_{het} > 0.1$ i.e., strong selection against protein-truncating variants.
3. High missense Z-score [64]: 1,440 constrained genes strongly depleted for missense mutations, with exp_syn ≥ 5, syn_z_sign < 3.09, and mis_z_sign > 3.09, as retrieved in Lek et al [62].
4. High Phi [65]: 588 LoF-constrained genes with a probability of haploinsufficiency (Phi) > 0.95.
5. MGI essential genes [66–68]: 2371 genes for which a homozygous knockout resulted in pre-, peri-, post-natal lethality
6. eQTL deficient [69]: 604 genes with no significant variant-gene association in all 48 tissues in GTEx v.7 single-tissue cis-eQTL data.
7. OMIM [70]: 2,266 genes deposited in the Online Mendelian Inheritance in Man (OMIM), as retrieved in Petrovski et al [71].
8. ClinVar [72]: 5,428 genes with a pathogenic or likely pathogenic variant with no conflict among studies.
9. DrugBank [73]: 373 genes whose protein products are human targets of FDA-approved drugs with known mechanisms of action.

The complete list of genes belonging to each of these categories is provided in **Additional File 8: Supp. Table VII**. We computed the expected and standard error of excess overlap between genes in each bin G^{i}_{b} for $i = 1, 2, 3, 4, 5$ and the reference gene set j, G^{j}_{r} using Eqn. 21 - 24, where G_{tot} represents all network nodes.

$$P_d = \frac{|G_r^{\,j} \cap G_b^{\,i}|}{|\,G_b^{\,i}|} \qquad \text{Eqn. 21}$$

$$P_{tot} = \frac{|G_r^{j} \cap G_{tot}|}{|\,G_{tot}|} \qquad \text{Eqn. 22}$$

$$excess\ overlap\ (G_b^{i},\ G_r^{j}) = \frac{P_d}{P_{tot}} \qquad \text{Eqn. 23}$$

$$SE\ excess\ overlap\ (G_b^{i},\ G_r^{j}) = \sqrt{\frac{P_d(1-P_d)}{|G_b^{i}|}}\ /\ P_{tot} \qquad \text{Eqn. 24}$$

L. Identifying biological processes associated with shared and distinct hub genes from non-cancer and cancer consensus network

In accordance with the scale-free criterion we selected the non-cancer network inferred using a penalization parameter λ = 0.18 resulting in a network density of 7355 edges and the cancer consensus network corresponding to the penalization parameter λ = 0.24 and a network density of 7552 edges to compare the biological processes which are represented by shared and distinct network hubs. First, we defined hub genes as network nodes with a closeness centrality in the 90th percentile independently for each consensus network, such that the non-cancer hub genes are given by H_N and the cancer hub genes are given by H_C. We then identified hub genes shared between cancer and non-cancer consensus networks $H_S = H_N \cap H_C$, non-cancer specific hub genes $H_{NS} = H_N \cap H_C'$, and cancer-specific hub genes as $H_{CS} = H_C \cap H_N'$ (**Additional**

File 10: Supp. Table IX). We then used the `GOTermFinder` tool [74] to identify GO terms that are shared by the genes in the sets H_S, H_{NS}, and H_{CS}.

M. Examining the differences in the degree distribution of tissue-specific vs. general transcription factors in consensus and context-specific networks

We selected context-specific networks inferred from CNS, blood, cardiac, skin, lung, skeletal muscle, and pancreas samples from *recount3* which had an approximate density of 7,000 edges (**Additional File 21: Supp. Table XVI**). Additionally, we selected values of the penalization parameter λ which yielded universal and non-cancer consensus networks with an approximate density of 7,000 edges. We referred to Pierson et al. [36] to obtain a list of tissue-specific and general transcription factors which are provided in **Additional File 9: Supp. Table VIII**. In order to select a background set of non-TFs, we first obtained the intersection of genes which were included in each network considered, then we excluded both general and tissue-specific TFs from this list, and randomly select 100 of these genes. The selected background is provided in **Additional File 9: Supp. Table VIII**. For each network, we compared the degree distribution of tissue-specific and general transcription factors to non-TFs and the degree distribution of tissue-specific to general transcription factors using the Wilcoxon rank-sum test. Across all tests, we adjusted for multiple hypothesis correction using the Holm-Bonferroni method.

N. Non-negative matrix factorization to determine shared co-regulatory relationships in similar tissues

We selected context-specific networks with a density of ~7000 across 27 contexts for which we inferred GCNs by aggregating samples assigned to the context from *recount3* (**Additional File 21: Supp. Table XVI**). Further, the selected networks were in accordance with the scale-free selection criterion detailed in **Methods (Section H)**. For each network, we identified hub genes as network nodes with a degree centrality in the 95th percentile. Across the 27 contexts, we found 3682 unique hubs. We subset to hubs that are present in at least 2 contexts which results in 1956 hubs. We then used the R package `RcppML` to perform non-negative matrix factorization to learn 8 underlying factors to group similar patterns of hub genes. Specifically, H is a binary matrix of dimensions $N_{Hubs} \times N_c$, where N_c is 27 the number of contexts. $H_{i,j} = 1$ when the i^{th} gene is a hub gene in context j and $H_{i,j} = 0$ otherwise. We then obtain matrices W of dimensions $N_{Hubs} \times 8$, and C of dimensions $N_c \times 8$ by solving the following optimization function,

$$min\,||H - WC^T|| \text{ such that } W \geq 0,\ C \geq 0 \qquad \text{Eqn. 25}$$

Finally, we chose a solution after 10 iterations that resulted in the greatest sparsity, i.e. smallest values of $||W||_1$ and $||C||_1$. To interpret the resulting context cluster, we examine the genes that contributed the most to the corresponding factor. Specifically, for a given factor, $W[:\,,p]$, we first obtain genes with loadings in the 80% percentile. Then for each gene, we compute the maximum difference between the loading of the gene on factor p to all other factors and select genes where this difference is ≥ 5e-5. Thus we obtain a set of factor-specific hub genes G_p (**Additional File 12: Supp. Table X**). We then used the `GOTermFinder` tool [74] to identify GO terms that were more likely to be present in the set G_p than a background of all protein-coding genes by estimating the odds ratio and p-value by applying the hypergeometric test.

O. Stratified LD-Score regression to quantify the heritability enrichment of variants proximal to central network genes in consensus and context-specific networks

We applied stratified LD-score regression (s-LDSC) [21] to quantify the contribution of node centrality estimated from our consensus and context-specific GCNs towards explaining complex-trait heritability. First, we transformed all centrality scores derived from our universal consensus, non-cancer consensus, blood and CNS context-specific networks to lie between 0 and 1. Next, we annotated SNPs within 100 Kb of a gene with the centrality score assigned to the gene. If an SNP was within 100 Kb of more than one gene, we assigned the maximum centrality score across all corresponding genes to the SNP. We generated six network centrality-based annotations **(Methods, Section I)** corresponding to each network studied and estimated their heritability enrichment and the standardized effect size (τ_c*) of an annotation c as described by S. Kim et. al [40].

Given an SNP j with a trait-specific effect size of β_j and a corresponding annotation value $a_{c,j}$ pertaining to category c, the variance of the effect size β_j is assumed to be a linear additive combination of the annotation c as given by Eqn. 25.

$$var(\beta_j) = \sum_c a_{c,j}\tau_c \qquad \text{Eqn. 25}$$

Here τ_c is the per-SNP contribution of the category c to the heritablity of the trait. s-LDSC then estimates τ_c using the regression model specified by Eqn. 26.

$$E[\chi_j^2] = N\sum_c l(j, c)\tau_c + 1 \qquad \text{Eqn. 26}$$

Where N is the number of samples in the GWAS and $l(j, c)$ is the LD score of SNP j to the annotation c computed as given by Eqn. 27.

$$l(j, c) = \sum_k a_{c,k} r^2_{j,k} \qquad \text{Eqn. 27}$$

Where $a_{c,k}$ is the annotation value of SNP k and $r^2_{j,k}$ is the correlation between SNPs j and k. We can then compute the enrichment of an annotation as the proportion of heritability explained by SNPs in a given annotation divided by the proportion of SNPs in the annotation. This definition can be extended to continuous annotations as given by Eqn. 28.

$$\text{Enrichment} = \frac{\% h_g^2(c)}{\% SNP\ (c)} = \frac{h_g^2(c) . M}{\sum_j a_{c,j} . h_g^2} \qquad \text{Eqn. 28}$$

Where $h_g^2(c)$ is the heritability captured by the c^{th} annotation, h_g^2 is the estimated SNP-heritability and M is the total number of SNPs used to compute h_g^2 which in this case is 5,961,159. When the annotation is enriched for trait heritability, the computed enrichment is > 1. To compute the significance of the enrichment, we used the block jack-knife method presented in previous studies [21, 40, 75, 76].

Finally, we computed the standardized effect size $\tau_c{}^*$ i.e. the proportionate change in the per-SNP heritability associated with a single standard deviation increase in the value of the annotation c conditioned on all other annotations in the model as given by Eqn. 29.

$$\tau_c{}^* = \frac{\tau_c\, sd\,(c)}{h_g^2 / M} \qquad \text{Eqn. 29}$$

Where $sd(c)$ is the standard deviation of the annotation c. $\tau_c{}^*$ thus captures the effect unique to the focal annotation, c unlike enrichment. The significance for the effect size of each annotation is computed by assuming $\tau_c{}^* \,/\, se(\tau_c{}^*) \sim N(0,\ 1)$ as done previously [40, 75, 77].

We used European samples from the 1000G phase 3 project [49] to obtain reference SNPs. Regression SNPs were obtained from HapMap 3 [78] and regression weights were obtained excluding SNPs in the major histocompatibility complex (MHC) from 1000G_Phase3_weights_hm3_no_MHC.tgz . We estimated heritability enrichment and annotation effect size $\tau_c{}^*$, using two model settings. In the first, we included annotations corresponding to variants located in a 100 Kb window of all protein-coding genes (all-genes annotation), in the second setting we included annotations corresponding to variants located in a 100 Kb window of all protein-coding genes and 97 annotations present in the baseline-LD model v2.2 (all-genes + baseline). Specifically, we downloaded the 1000G_Phase3_baselineLD_v2.2_ldscores.tgz file which included 97 variant annotations such as the annotations provided by Gazal et. al [79], Hujoel et. al [80], promoter and enhancer specific annotations from Villar et. al [81], and promoter and enhancer age annotations from Marnetto et. al [82].

To examine the heritability enrichment and effect size of annotations derived from the universal and non-cancer consensus networks which were selected based on the scale-free distribution of node degree detailed in **Methods (Section H)** we used two sets of traits.

1. 42 traits considered by S. Kim et al, such that the Z-score of total SNP-heritability was at least 6 and the genetic correlation between any pair of traits estimated by cross-trait LDSC was lower than 0.9. A complete list of traits is provided in **Additional File 15: Supp. Table XI**
2. 219 UKBB traits with a heritability Z-score >= 7, and the genetic correlation estimated by cross-trait LDSC is lower than 0.5. A complete list of traits is provided in **Additional File 16: Supp. Table XII**.

To examine the heritability enrichment of blood context-specific networks derived from samples solely from GTEx and inferred across all aggregated samples we utilized GWAS summary statistics corresponding to 9 blood-derived traits including, ulcerative colitis [83], rheumatoid arthritis [84], and Crohn’s disease [83], as well as eczema, white cell count, red cell count, red blood cell width, platelet count, eosinophil count from UKBB (**Additional File 17: Supp. Table XII**). Networks derived from blood samples were selected based on the scale-free criterion for node degree distribution detailed in **Methods (Section H)**.

To examine the heritability of CNS context-specific networks derived from samples solely from GTEx and inferred across all aggregated samples we utilized GWAS summary statistics from the Psychiatric Genomics Consortium [85] corresponding to Alzheimer’s disease [86], epilepsy [87], Parkinson's, bipolar disorder [88], smoking cessation [89], schizophrenia [90], major depressive disorder [91], number of drinks per week [89], and waist-hip-ratio adjusted BMI from UKBB (**Additional File 18: Supp. Table XIV**). Networks derived from CNS samples were selected based on the scale-free criterion for node degree distribution detailed in **Methods (Section H)**. Following the computation of heritability enrichment and $\tau_c{}^*$ for each trait, as well as their respective standard deviations we performed a random-effects meta-analysis across traits by using the function `meta.summaries()` from the R package `rmeta`.

Ethics Declarations

Ethics approval and consent to participate

Ethical approval is not applicable for this manuscript.

Consent for publication

Consent for publication is not applicable for this manuscript.

Availability of data and materials

Scripts to reproduce the analysis and figures included in this manuscript can be found at: https://github.com/prashanthi-ravichandran/recount3_networks

Networks and annotations used in this project can be obtained from: **10.5281/zenodo.10480999**

Competing interests

A.B. is a consultant for Third Rock Ventures, LLC, a shareholder in Alphabet, Inc, and a founder of CellCipher, Inc.

Funding

Alexis Battle was supported by NIH/NIGMS R35GM139580. Kaspar Hansen and Alexis Battle were supported by NIH/NIGMS R01GM121459.

Authors' contributions

P.R., P.P.., and A.B. conceived the project. P.R., P.P., and A.B. designed the analyses. P.R. and P.P. performed the analyses. R.K. and K.H. contributed feedback to experimental design and interpretation. P.R., R.K., and A.B. organized and wrote the paper with input from all authors.

Acknowledgements

The authors would like to thank helpful discussions from Battle lab members throughout the course of this work, particularly Joshua Weinstock and Eric Kernfeld for code review and manuscript feedback.

Supplementary Information

Additional File 1: Supp. Table I
Assignment of tissue labels obtained by manual curation to 48 contexts.

Additional File 2: Supp. Fig 1 - 19
Supp. Fig 1. Identification of outlier samples across contexts. **Supp. Fig 2.** Immune cells were separated into three clusters: Melyoid, PBMCs/T cells, and B cells. **Supp. Fig 3.** Comparison of GTEx to Tissue consensus networks across tissue contexts. **Supp. Fig 4.** Characteristics of PCs at varying levels of data aggregation. **Supp. Fig 5.** ANOVA of top 10 PCs at varying levels of data aggregation. **Supp. Fig 6.** Prevalence of tissues in GTEx and SRA. **Supp. Fig 7.** Held-out Log-likelihood calculated reciprocally for GTEx and SRA. **Supp. Fig 8.** F1 scores calculated reciprocally for GTEx and SRA. **Supp. Fig 9.** Regression estimate (β) and standard errors of the effect of sample size (N) on network density across varying penalization parameters λ. **Supp. Fig 10.** Held-out log-likelihood of networks inferred by sequential data aggregation of GTEx and SRA studies. **Supp. Fig 11.** Linear model between the log empirical degree distribution and log degree for consensus networks. **Supp. Fig 12.** Odds ratio for ubiquitous biological processes across networks. **Supp. Fig 13.** Odds ratio for tissue specific biological processes across networks. **Supp. Fig 14.** Excess overlap of functional gene sets across networks. **Supp. Fig 15.** Excess overlap of functional gene sets across context-specific networks. **Supp. Fig 16.** S-LDSC results meta-analyzed across 42 traits for annotations from consensus networks. **Supp. Fig 17.** S-LDSC results meta-analyzed across 219 UKBB traits for annotations from consensus

networks. **Supp. Fig 18.** S-LDSC results meta-analyzed across 9 blood traits. **Supp. Fig 19.** S-LDSC results meta-analyzed across 9 CNS traits.

Additional File 3: Supp. Table II: Details pertaining to the number of samples, median sample size across aggregated studies , number of PCs regressed when data is aggregated prior to correction for technical, and median number of PCs regressed from each study prior to aggregation for sequential aggregation of 566 non-cancerous studies from SRA and 49 studies from GTEx.

Additional File 4: Supp. Table III: Specification of data sources used in the compilation of pathways including the number of gene sets obtained from each source.

Additional File 5: Supp. Table IV: Selection of penalization parameter Lambda for consensus networks based on the scale-free criterion for degree distribution.

Additional File 6: Supp. Table V: Selection of penalization parameter Lambda for context-specific networks based on the scale-free criterion for degree distribution.

Additional File 7: Supp. Table VI: Details of GO terms that were tested for enrichment as a function of degree thresholds in consensus and context-specific networks.

Additional File 8: Supp. Table VII: Details of evolutionarily constrained and functional gene sets for which excess overlap is computed across network nodes binned by degree centrality.

Additional File 9: Supp. Table VIII: List of general and tissue-specific transcription factors derived from Pierson. et. al, as well as randomly selected background genes used to evalute the differences in the centrality scores obtained from consensus and context-specific networks

Additional File 10: Supp. Table IX: Hub genes that are shared and distinct between non-cancer consensus network with 11,110 edges ($\lambda = 0.16$) and the cancer consensus network with 10,482 edges ($\lambda = 0.22$).

Additional File 11: Supplementary File 1: Enrichment of GO terms in cancer-specific hub genes.

Additional File 12: Supp. Table X: Hub genes selected to describe each factor such that, the loading of the gene on the factor was in the 80th percentile, and the minimum difference between the weight of the gene on the selected factor and all other factors is >= 5e-5.

Additional File 13: Supplementary File 2: Enrichment of GO terms among hub genes which are specific to Factor 7 which results in the grouping of PBMCs/ T cells.

Additional File 14: Supplementary File 3: Enrichment of GO terms among hub genes which are specific to Factor 6 which results in the grouping of hESCs, iPSCs, and multipotent cells.

Additional File 15: Supp. Table XI: 42 Independent traits examined by S.Kim et. al, and their corresponding references, heritability, Z-score and number of individuals in the GWAS

Additional File 16: Supp. Table XII: 219 UKBB traits that are selected based on having a Z-score >= 7, and pairwise correlation between traits is lesser than or equal to 0.5 as estimated by LDSC.

Additional File 17: Supp. Table XIII: 9 blood-related traits which were used to examine heritability enrichment of blood specific networks.

Additional File 18: Supp. Table XIV: 9 CNS-related traits which were used to examine heritability enrichment of CNS specific networks.

Additional File 19: Supplementary File 4: Manually curated annotations corresponding to tissue, cancer status and disease type of SRA samples based on text-based analysis of Study, Tissue, Organ, Biopsy, Cell, Disease, Source and Description from the metadata sample_description field.

Additional File 20: Supp. Table XV: Mapping between annotation categories present in tissue-specific PPI interactions obtained from SNAP and contexts across which context-specific networks were inferred.

Additional File 21: Supp. Table XVI: Selection of context-specific networks used in matrix factorization of shared hubs and edges.

References

1. Hartwell LH, Hopfield JJ, Leibler S, Murray AW (1999) From molecular to modular cell biology. Nature 402:C47–52

2. Hasty J, McMillen D, Collins JJ (2002) Engineered gene circuits. Nature 420:224–230

3. Oltvai ZN, Barabási A-L (2002) Systems biology. Life’s complexity pyramid. Science 298:763–764

4. Alon U (2003) Biological networks: the tinkerer as an engineer. Science 301:1866–1867

5. Stuart JM, Segal E, Koller D, Kim SK (2003) A Gene-Coexpression Network for Global Discovery

of Conserved Genetic Modules. Science. https://doi.org/10.1126/science.1087447

6. Schlitt T, Palin K, Rung J, Dietmann S, Lappe M, Ukkonen E, Brazma A (2003) From gene networks to gene function. Genome Res 13:2568–2576

7. Narang V, Ramli MA, Singhal A, Kumar P, de Libero G, Poidinger M, Monterola C (2015) Automated Identification of Core Regulatory Genes in Human Gene Regulatory Networks. PLoS Comput Biol 11:e1004504

8. Wang X, Choi D, Roeder K (2021) Constructing local cell-specific networks from single-cell data. Proc Natl Acad Sci U S A. https://doi.org/10.1073/pnas.2113178118

9. van Dam S, Võsa U, van der Graaf A, Franke L, de Magalhães JP (2017) Gene co-expression analysis for functional classification and gene–disease predictions. Brief Bioinform 19:575–592

10. Diaz LPM, Stumpf MPH (2022) Gaining confidence in inferred networks. Sci Rep. https://doi.org/10.1038/s41598-022-05402-9

11. Segal E, Shapira M, Regev A, Pe’er D, Botstein D, Koller D, Friedman N (2003) Module networks: identifying regulatory modules and their condition-specific regulators from gene expression data. Nat Genet. https://doi.org/10.1038/ng1165

12. Wolf DM, Lenburg ME, Yau C, Boudreau A, van ‘t Veer LJ (2014) Gene Co-Expression Modules as Clinically Relevant Hallmarks of Breast Cancer Diversity. PLoS One. https://doi.org/10.1371/journal.pone.0088309

13. Friedman J, Hastie T, Tibshirani R (2008) Sparse inverse covariance estimation with the graphical lasso. Biostatistics 9:432–441

14. Hastie T, Tibshirani R, Friedman J (2013) The Elements of Statistical Learning: Data Mining, Inference, and Prediction. Springer Science & Business Media

15. Huang Y-J, Lu T-P, Hsiao CK (2020) Application of graphical lasso in estimating network structure in gene set. Annals of Translational Medicine. https://doi.org/10.21037/atm-20-6490

16. Wilks C, Zheng SC, Chen FY, et al (2021) recount3: summaries and queries for large-scale RNA-seq expression and splicing. Genome Biol 22:323

17. Consortium TG, The GTEx Consortium (2020) The GTEx Consortium atlas of genetic regulatory effects across human tissues. Science 369:1318–1330

18. Tomczak K, Czerwińska P, Wiznerowicz M (2015) The Cancer Genome Atlas (TCGA): an immeasurable source of knowledge. Contemp Oncol 19:A68–77

19. Katz K, Shutov O, Lapoint R, Kimelman M, Brister JR, O’Sullivan C (2022) The Sequence Read Archive: a decade more of explosive growth. Nucleic Acids Res 50:D387–D390

20. Kodama Y, Shumway M, Leinonen R, on behalf of the International Nucleotide Sequence Database Collaboration (2012) The sequence read archive: explosive growth of sequencing data. Nucleic Acids Research 40:D54–D56

21. Finucane HK, Bulik-Sullivan B, Gusev A, et al (2015) Partitioning heritability by functional annotation using genome-wide association summary statistics. Nat Genet 47:1228–1235

22. Aran D, Hu Z, Butte AJ (2017) xCell: digitally portraying the tissue cellular heterogeneity landscape. Genome Biol 18:220

23. Leek JT, Evan Johnson W, Parker HS, Jaffe AE, Storey JD (2012) The sva package for removing batch effects and other unwanted variation in high-throughput experiments. Bioinformatics 28:882–883

24. Parsana P, Ruberman C, Jaffe AE, Schatz MC, Battle A, Leek JT (2019) Addressing confounding artifacts in reconstruction of gene co-expression networks. Genome Biol 20:94

25. Buja A, Eyuboglu N (1992) Remarks on Parallel Analysis. Multivariate Behav Res 27:509–540

26. Kanehisa M, Goto S (2000) KEGG: kyoto encyclopedia of genes and genomes. Nucleic Acids Res 28:27–30

27. Schaefer CF, Anthony K, Krupa S, Buchoff J, Day M, Hannay T, Buetow KH (2009) PID: the Pathway Interaction Database. Nucleic Acids Res 37:D674–9

28. Chen EY, Tan CM, Kou Y, Duan Q, Wang Z, Meirelles GV, Clark NR, Ma'ayan A (2013) Enrichr: interactive and collaborative HTML5 gene list enrichment analysis tool. BMC Bioinformatics 14:128

29. Kuleshov MV, Jones MR, Rouillard AD, et al (2016) Enrichr: a comprehensive gene set enrichment analysis web server 2016 update. Nucleic Acids Res 44:W90–7

30. Leskovec J, Sosič R (2016) SNAP: A General Purpose Network Analysis and Graph Mining Library. ACM Trans Intell Syst Technol. https://doi.org/10.1145/2898361

31. Ha MJ, Baladandayuthapani V, Do K-A (2015) DINGO: differential network analysis in genomics. Bioinformatics 31:3413–3420

32. Pastor-Satorras R, Rubi M, Diaz-Guilera A (2003) Statistical Mechanics of Complex Networks. Springer Science & Business Media

33. Chou W-C, Cheng A-L, Brotto M, Chuang C-Y (2014) Visual gene-network analysis reveals the cancer gene co-expression in human endometrial cancer. BMC Genomics 15:300

34. Oh E-Y, Christensen SM, Ghanta S, et al (2015) Extensive rewiring of epithelial-stromal co-expression networks in breast cancer. Genome Biol 16:128

35. Albert R (2005) Scale-free networks in cell biology. Journal of Cell Science 118:4947–4957

36. Pierson E, GTEx Consortium, Koller D, et al (2015) Sharing and Specificity of Co-expression Networks across 35 Human Tissues. PLoS Comput Biol 11:e1004220

37. Rodius S, Fournier A, Götz L, et al (2016) Analysis of the dynamic co-expression network of heart regeneration in the zebrafish. Sci Rep 6:26822

38. Keller MP, Choi Y, Wang P, et al (2008) A gene expression network model of type 2 diabetes links cell cycle regulation in islets with diabetes susceptibility. Genome Res 18:706–716

39. Presson AP, Sobel EM, Papp JC, Suarez CJ, Whistler T, Rajeevan MS, Vernon SD, Horvath S (2008) Integrated weighted gene co-expression network analysis with an application to chronic fatigue

syndrome. BMC Syst Biol 2:95

40. Kim SS, Dai C, Hormozdiari F, et al (2019) Genes with High Network Connectivity Are Enriched for Disease Heritability. Am J Hum Genet 105:1302

41. Mostafavi H, Spence JP, Naqvi S, Pritchard JK (2022) Limited overlap of eQTLs and GWAS hits due to systematic differences in discovery. bioRxiv 2022.05.07.491045

42. Zhu X, Duren Z, Wong WH (2021) Modeling regulatory network topology improves genome-wide analyses of complex human traits. Nat Commun 12:1–15

43. Cote AC, Young HE, Huckins LM (2022) Comparison of confound adjustment methods in the construction of gene co-expression networks. Genome Biol 23:44

44. Stegle O, Parts L, Piipari M, Winn J, Durbin R (2012) Using probabilistic estimation of expression residuals (PEER) to obtain increased power and interpretability of gene expression analyses. Nat Protoc 7:500–507

45. Ju JH, Shenoy SA, Crystal RG, Mezey JG (2017) An independent component analysis confounding factor correction framework for identifying broad impact expression quantitative trait loci. PLoS Comput Biol 13:e1005537

46. Luijk R, Dekkers KF, van Iterson M, et al (2018) Genome-wide identification of directed gene networks using large-scale population genomics data. Nat Commun 9:3097

47. Deelen P, Zhernakova DV, de Haan M, et al (2015) Calling genotypes from public RNA-sequencing data enables identification of genetic variants that affect gene-expression levels. Genome Med 7:30

48. Omranian N, Eloundou-Mbebi JMO, Mueller-Roeber B, Nikoloski Z (2016) Gene regulatory network inference using fused LASSO on multiple data sets. Sci Rep 6:20533

49. Hellstern M, Ma J, Yue K, Shojaie A (2021) netgsa: Fast computation and interactive visualization for topology-based pathway enrichment analysis. PLoS Comput Biol 17:e1008979

50. Margolin AA, Nemenman I, Basso K, Wiggins C, Stolovitzky G, Favera RD, Califano A (2006) ARACNE: An Algorithm for the Reconstruction of Gene Regulatory Networks in a Mammalian Cellular Context. BMC Bioinformatics 7:1–15

51. Opgen-Rhein R, Strimmer K (2007) From correlation to causation networks: a simple approximate learning algorithm and its application to high-dimensional plant gene expression data. BMC Syst Biol 1:37

52. Babaei S, Mahfouz A, Hulsman M, Lelieveldt BPF, de Ridder J, Reinders M (2015) Hi-C Chromatin Interaction Networks Predict Co-expression in the Mouse Cortex. PLoS Comput Biol 11:e1004221

53. Zhou K-R, Liu S, Sun W-J, Zheng L-L, Zhou H, Yang J-H, Qu L-H (2016) ChIPBase v2.0: decoding transcriptional regulatory networks of non-coding RNAs and protein-coding genes from ChIP-seq data. Nucleic Acids Res 45:D43–D50

54. Dixit A, Parnas O, Li B, et al (2016) Perturb-Seq: Dissecting Molecular Circuits with Scalable Single-Cell RNA Profiling of Pooled Genetic Screens. Cell 167:1853–1866.e17

55. Battle A (2019) Pre-computed cross-mappability resources for human genomes (hg19 and GRCh38).

https://doi.org/10.6084/m9.figshare.c.4297352.v4

56. Saha A, Battle A (2018) False positives in trans-eQTL and co-expression analyses arising from RNA-sequencing alignment errors. F1000Res 7:1860

57. Zitnik M, Leskovec J (2017) Predicting multicellular function through multi-layer tissue networks. Bioinformatics 33:i190–i198

58. Greene CS, Krishnan A, Wong AK, et al (2015) Understanding multicellular function and disease with human tissue-specific networks. Nat Genet 47:569–576

59. Chang A, Schomburg I, Placzek S, Jeske L, Ulbrich M, Xiao M, Sensen CW, Schomburg D (2015) BRENDA in 2015: exciting developments in its 25th year of existence. Nucleic Acids Res 43:D439–46

60. van Noort V, Snel B, Huynen MA (2004) The yeast coexpression network has a small−world, scale−free architecture and can be explained by a simple model. EMBO reports 5:280–284

61. Resendis-Antonio O, Freyre-González JA, Menchaca-Méndez R, Gutiérrez-Ríos RM, Martínez-Antonio A, Avila-Sánchez C, Collado-Vides J (2005) Modular analysis of the transcriptional regulatory network of E. coli. Trends Genet 21:16–20

62. Lek M, Karczewski KJ, Minikel EV, et al (2016) Analysis of protein-coding genetic variation in 60,706 humans. Nature 536:285–291

63. Cassa CA, Weghorn D, Balick DJ, et al (2017) Estimating the selective effects of heterozygous protein-truncating variants from human exome data. Nat Genet 49:806–810

64. Samocha KE, Robinson EB, Sanders SJ, et al (2014) A framework for the interpretation of de novo mutation in human disease. Nat Genet 46:944–950

65. Bartha I, Rausell A, McLaren PJ, Mohammadi P, Tardaguila M, Chaturvedi N, Fellay J, Telenti A (2015) The Characteristics of Heterozygous Protein Truncating Variants in the Human Genome. PLoS Comput Biol 11:e1004647

66. Blake JA, Bult CJ, Kadin JA, Richardson JE, Eppig JT, Mouse Genome Database Group (2011) The Mouse Genome Database (MGD): premier model organism resource for mammalian genomics and genetics. Nucleic Acids Res 39:D842–8

67. Georgi B, Voight BF, Bućan M (2013) From mouse to human: evolutionary genomics analysis of human orthologs of essential genes. PLoS Genet 9:e1003484

68. Liu X, Jian X, Boerwinkle E (2013) dbNSFP v2.0: a database of human non-synonymous SNVs and their functional predictions and annotations. Hum Mutat 34:E2393–402

69. GTEx Consortium, Laboratory, Data Analysis &Coordinating Center (LDACC)—Analysis Working Group, Statistical Methods groups—Analysis Working Group, et al (2017) Genetic effects on gene expression across human tissues. Nature 550:204–213

70. Hamosh A, Scott AF, Amberger JS, Bocchini CA, McKusick VA (2005) Online Mendelian Inheritance in Man (OMIM), a knowledgebase of human genes and genetic disorders. Nucleic Acids Res 33:D514–7

71. Petrovski S, Wang Q, Heinzen EL, Allen AS, Goldstein DB (2013) Genic intolerance to functional variation and the interpretation of personal genomes. PLoS Genet 9:e1003709

72. Landrum MJ, Lee JM, Benson M, et al (2018) ClinVar: improving access to variant interpretations and supporting evidence. Nucleic Acids Res 46:D1062–D1067

73. Wishart DS, Feunang YD, Guo AC, et al (2018) DrugBank 5.0: a major update to the DrugBank database for 2018. Nucleic Acids Res 46:D1074–D1082

74. Boyle EI, Weng S, Gollub J, Jin H, Botstein D, Cherry JM, Sherlock G (2004) GO::TermFinder--open source software for accessing Gene Ontology information and finding significantly enriched Gene Ontology terms associated with a list of genes. Bioinformatics 20:3710–3715

75. Hormozdiari F, Gazal S, van de Geijn B, et al (2018) Leveraging molecular quantitative trait loci to understand the genetic architecture of diseases and complex traits. Nat Genet 50:1041–1047

76. Finucane HK, Reshef YA, Anttila V, et al (2018) Heritability enrichment of specifically expressed genes identifies disease-relevant tissues and cell types. Nat Genet 50:621–629

77. Gazal S, Finucane HK, Furlotte NA, et al (2017) Linkage disequilibrium-dependent architecture of human complex traits shows action of negative selection. Nat Genet 49:1421–1427

78. International HapMap 3 Consortium, Altshuler DM, Gibbs RA, et al (2010) Integrating common and rare genetic variation in diverse human populations. Nature 467:52–58

79. Gazal S, Loh P-R, Finucane HK, Ganna A, Schoech A, Sunyaev S, Price AL (2018) Functional architecture of low-frequency variants highlights strength of negative selection across coding and non-coding annotations. Nat Genet 50:1600–1607

80. Hujoel MLA, Gazal S, Hormozdiari F, van de Geijn B, Price AL (2019) Disease Heritability Enrichment of Regulatory Elements Is Concentrated in Elements with Ancient Sequence Age and Conserved Function across Species. Am J Hum Genet. https://doi.org/10.1016/j.ajhg.2019.02.008

81. Villar D, Berthelot C, Aldridge S, et al (2015) Enhancer evolution across 20 mammalian species. Cell 160:554–566

82. Marnetto D, Mantica F, Molineris I, Grassi E, Pesando I, Provero P (2018) Evolutionary Rewiring of Human Regulatory Networks by Waves of Genome Expansion. Am J Hum Genet 102:207–218

83. Jostins L, Ripke S, Weersma RK, et al (2012) Host-microbe interactions have shaped the genetic architecture of inflammatory bowel disease. Nature 491:119–124

84. Okada Y, Wu D, Trynka G, et al (2014) Genetics of rheumatoid arthritis contributes to biology and drug discovery. Nature 506:376–381

85. Sullivan PF, Agrawal A, Bulik CM, et al (2018) Psychiatric Genomics: An Update and an Agenda. Am J Psychiatry 175:15–27

86. Jansen IE, Savage JE, Watanabe K, et al (2019) Genome-wide meta-analysis identifies new loci and functional pathways influencing Alzheimer's disease risk. Nat Genet 51:404–413

87. International League Against Epilepsy Consortium on Complex Epilepsies. Electronic address:

epilepsy-austin@unimelb.edu.au (2014) Genetic determinants of common epilepsies: a meta-analysis of genome-wide association studies. Lancet Neurol 13:893–903

88. Stahl EA, Breen G, Forstner AJ, et al (2019) Genome-wide association study identifies 30 loci associated with bipolar disorder. Nat Genet 51:793–803

89. Liu M, Jiang Y, Wedow R, et al (2019) Association studies of up to 1.2 million individuals yield new insights into the genetic etiology of tobacco and alcohol use. Nat Genet 51:237–244

90. (2019) GENOMIC DISSECTION OF BIPOLAR DISORDER AND SCHIZOPHRENIA IN 50K CASES, 50K CONTROLS AND 28 SUBPHENOTYPES. Eur Neuropsychopharmacol 29:S814–S815

91. Wray NR, Ripke S, Mattheisen M, et al (2018) Genome-wide association analyses identify 44 risk variants and refine the genetic architecture of major depression. Nat Genet 50:668–681

Figure Legends

Fig. 1

Overview of data pre-processing and annotations (A) Gene expression data was RPKM normalized and log-transformed along with gene-specific and sample-specific filters. Based on the data source, normalized gene expression was processed to merge replicates, and exclude miRNA and scRNA seq samples. **(B)** Number of samples which were annotated to be non-cancer, cancer, and unknown based on available metadata across GTEx, SRA, and TCGA. **(C)** Top 10 tissue labels by sample size across all three data sources: SRA, GTEx, and TCGA. **(D)** Top 20 diseases by sample size found in SRA that are not cancer. **(E)** t-SNE projection of xCell deconvolution scores of 63,193 non-cancerous samples colored by the tissue of origin. **(F)** Increase in the sample size of 27 tissue contexts by using SRA samples compared to GTEx only. SRA studies included 7 novel contexts which were not available in GTEx.

Fig. 2

Comparison of aggregation strategies to optimize network reconstruction (A) Outline of strategies to compare data correction before and after aggregation and weighted and unweighted aggregation of single tissue/ study covariance matrices included (1) Aggregating data before PC-based data correction followed by estimation of empirical covariance from residual expression (Aggregating data, orange), (2) PC-based data correction applied to individual studies followed by aggregation of residual expression and joint estimation of empirical covariance (Aggregating data adjusted for confounding, brick red), (3) Unweighted aggregation of covariance matrices inferred from each study separately after study-specific PC-based correction (Unweighted covariance aggregation, purple) and (4) Weighted aggregation of covariance matrices computed from individual studies following study-specific PC-based data correction (Weighted covariance aggregation, magenta). **(B)** Held-out log-likelihood of networks inferred by sequentially aggregating either 10 GTEx studies or 100 SRA studies at a time. **(C)** F1-score of networks inferred by sequentially aggregating either 10 GTEx studies or 100 SRA studies at a time when compared to canonical pathways compiled from KEGG, Biocarta, and Pathway Interaction Database. **(D)** Comparison of held-out log-likelihood corresponding to networks inferred over 49 GTEx studies or 566 SRA studies using four different aggregation strategies including aggregating data, aggregating data adjusted for confounding, unweighted, and weighted aggregation of covariance matrices. **(E)** Comparison of F1-scores of obtaining edges corresponding to canonical pathways from KEGG, Biocarta, and Pathway Interaction Database in networks inferred over 49 GTEx studies or 566 SRA studies using four different aggregation strategies including aggregating data, aggregating data adjusted for confounding, unweighted, and weighted aggregation of covariance matrices. **(F)** Total number of samples, number of individual studies, and the median sample size of each study which were used in the inference of universal consensus, non-cancer consensus, and cancer consensus networks. **(G)** Comparison of F1-scores of obtaining edges corresponding to canonical pathways in the three consensus networks, universal, non-cancer, and cancer, across networks with density (*E*) varying between 5e3 to 5e6 edges. **(H)** Log-likelihood of GTEx blood samples based on networks inferred by sequentially aggregating SRA blood studies five at a time for densities ranging from 1e3 to 1e5 edges. **(I)** Log-likelihood of GTEx CNS samples based on networks inferred by sequentially aggregating SRA CNS studies five at a time for densities ranging from 1e3 to 1e5 edges. **(J)** Odds ratio of finding edges corresponding to tissue-specific protein-protein interactions (PPIs) derived from SNAP in tissue-context-specific networks inferred using all available samples vs. only samples found in GTEx for six tissue contexts.

Fig. 3

Properties of central network nodes of consensus and context-specific networks (A-C) Enrichment of genes involved in GO processes among network genes selected with increasing thresholds of degree connectivity in three consensus networks, universal ($\lambda = 0.18$, 7087 edges), non-cancer ($\lambda = 0.18$, 7355 edges), and cancer ($\lambda = 0.24$, 7552 edges), as well as two context-specific networks blood ($\lambda = 0.24$, 7283 edges) and CNS ($\lambda = 0.28$, 8430 edges). Tissue-context-specific networks were inferred only using non-cancerous samples. Blood (GTEx) or CNS (GTEx) networks were inferred using samples only found in GTEx while Blood and CNS networks were inferred using samples from GTEx and SRA. **(D)** Distribution of the excess overlap of evolutionarily conserved gene sets (Methods) for network nodes binned by the number of neighbors (degree) corresponding to universal consensus networks ($\lambda = 0.14, 0.16, 0.18, 0.20$), non-cancer consensus network ($\lambda = 0.14, 0.16, 0.18, 0.20$), cancer consensus networks (λ = 0.20, 0.22, 0.24, 0.26), blood network (λ = 0.18, 0.20, 0.22, 0.24, 0.26), and CNS network (λ = 0.24, 0.26, 0.28, 0.30, 0.32). Quintile 1 reflects nodes with no neighbors. Nodes with non-zero neighbors are split based on the degree quartile they belong to (Quintiles 2-5). We evaluated the excess overlap of 3,104 loss-of-function (LoF) genes with pLI > 0.9,2,853 genes with a $S_{het} > 0.1$, 588 genes with a Phi-score > 0.95, and 1,440 genes strongly depleted for missense mutations (high missense z-score). **(E)** The degree distribution of network nodes that are tissue-specific transcription factors (TFs) in blood (52 TFs), lung (58 TFs), skin (10 TFs), pancreas (16 TFs), cardiac (17 TFs), muscle (7 TFs), CNS (51 TFs), general transcription factors (88 TFs), and protein-coding genes which are not transcription factors in universal consensus (λ = 0.18, 7,087 edges), non-cancer consensus (λ = 0.18, 7,355 edges), skin (λ = 0.26, 7,567 edges), skeletal muscle (λ = 0.26, 6,254 edges), pancreas (λ = 0.32, 7,615 edges), lung (λ = 0.30, 6,349 edges), CNS (λ = 0.30, 6,316 edges), cardiac (λ = 0.30, 6,481 edges), blood (λ = 0.24, 7,283 edges). Pairs with no significance reported were not statistically distinct ($p > 0.1$). **(F)** Factor weights were obtained by non-negative matrix factorization of the presence of hub genes in tissue-specific networks with ~ 7,000 edges. Details of the penalization parameter λ and density of selected networks for each tissue context are provided in **Supp. Table X**.

Fig. 4

Heritability enrichment of network annotations Mean and standard deviation of heritability enrichment and the coefficient τ^*, an estimate of the heritability of SNPs unique to the annotation. All genes: whether a variant was located in a 100 kilobase window of all protein-coding genes, All genes + baseline: all-genes annotation in addition to 97 functional annotations such as known enhancer and promoter regions. **(A)** Meta-analysis of 42 independent traits for six centrality measures obtained from the universal consensus network and non-cancer consensus networks corresponding to values of the penalization parameter λ between 0.14 - 0.20. **(B)** Meta-analysis of 9 blood-related traits including, Crohn’s disease, Ulcerative colitis, Rheumatoid arthritis, Allergy Eczema, Eosinophil count, Red blood cell count, White blood cell count, Red blood cell width, and Platelet count for network annotations from Blood GTEx (λ = 0.24 - 0.32), Blood consensus (λ = 0.18 - 0.26), and Universal consensus network (λ = 0.14 - 0.20). **(C)** Meta-analysis of 9 CNS-related traits including, Alzheimer’s disease, Epilepsy, Parkinson’s disease, Bipolar disorder, Smoking cessation, Waist-hip-ratio adjusted BMI, Schizophrenia, Major depressive disorder, and Number of alcoholic drinks per week, for network annotations corresponding to 6 centrality measures derived from CNS GTEx (λ = 0.26 - 0.32), CNS (λ = 0.20 - 0.28), and Universal consensus network(λ = 0.14 - 0.20).

Figure 1

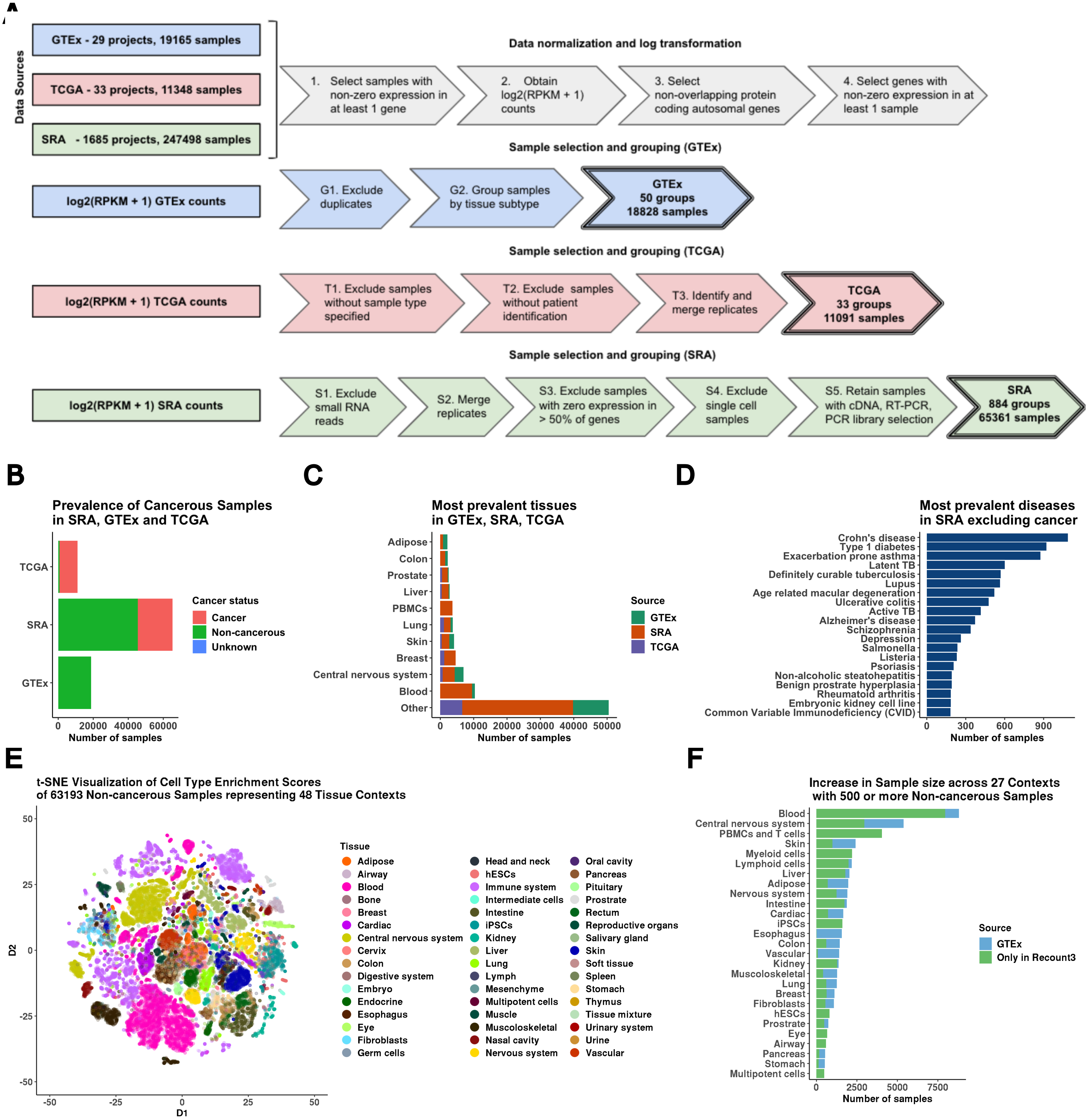
A
Data Sources
GTEx - 29 projects, 19165 samples
TCGA - 33 projects, 11348 samples
SRA - 1685 projects, 247498 samples
Data normalization and log transformation
1. Select samples with non-zero expression in at least 1 gene
2. Obtain log2(RPKM + 1) counts
3. Select non-overlapping protein coding autosomal genes
4. Select genes with non-zero expression in at least 1 sample
Sample selection and grouping (GTEx)
log2(RPKM + 1) GTEx counts
G1. Exclude duplicates
G2. Group samples by tissue subtype
GTEx 50 groups 18828 samples
Sample selection and grouping (TCGA)
log2(RPKM + 1) TCGA counts
T1. Exclude samples without sample type specified
T2. Exclude samples without patient identification
T3. Identify and merge replicates
TCGA 33 groups 11091 samples
Sample selection and grouping (SRA)
log2(RPKM + 1) SRA counts
S1. Exclude small RNA reads
S2. Merge replicates
S3. Exclude samples with zero expression in > 50% of genes
S4. Exclude single cell samples
S5. Retain samples with cDNA, RT-PCR, PCR library selection
SRA 884 groups 65361 samples
B
Prevalence of Cancerous Samples in SRA, GTEx and TCGA
TCGA
SRA
GTEx
0
20000
40000
60000
Number of samples
Cancer status
Cancer
Non-cancerous
Unknown
C
Most prevalent tissues in GTEx, SRA, TCGA
Adipose
Colon
Prostate
Liver
PBMCs
Lung
Skin
Breast
Central nervous system
Blood
Other
0
10000
20000
30000
40000
50000
Number of samples
Source
GTEx
SRA
TCGA
D
Most prevalent diseases in SRA excluding cancer
Crohn's disease
Type 1 diabetes
Exacerbation prone asthma
Latent TB
Definitely curable tuberculosis
Lupus
Age related macular degeneration
Ulcerative colitis
Active TB
Alzheimer's disease
Schizophrenia
Depression
Salmonella
Listeria
Psoriasis
Non-alcoholic steatohepatitis
Benign prostrate hyperplasia
Rheumatoid arthritis
Embryonic kidney cell line
Common Variable Immunodeficiency (CVID)
0
300
600
900
Number of samples
E
t-SNE Visualization of Cell Type Enrichment Scores of 63193 Non-cancerous Samples representing 48 Tissue Contexts
D2
50
25
0
-25
-50
-50
-25
0
25
50
D1
Tissue
Adipose
Airway
Blood
Bone
Breast
Cardiac
Central nervous system
Cervix
Colon
Digestive system
Embryo
Endocrine
Esophagus
Eye
Fibroblasts
Germ cells
Head and neck
hESCs
Immune system
Intermediate cells
Intestine
iPSCs
Kidney
Liver
Lung
Lymph
Mesenchyme
Multipotent cells
Muscle
Muscoloskeletal
Nasal cavity
Nervous system
Oral cavity
Pancreas
Pituitary
Prostrate
Rectum
Reproductive organs
Salivary gland
Skin
Soft tissue
Spleen
Stomach
Thymus
Tissue mixture
Urinary system
Urine
Vascular
F
Increase in Sample size across 27 Contexts with 500 or more Non-cancerous Samples
Blood
Central nervous system
PBMCs and T cells
Skin
Myeloid cells
Lymphoid cells
Liver
Adipose
Nervous system
Intestine
Cardiac
iPSCs
Esophagus
Colon
Vascular
Kidney
Muscoloskeletal
Lung
Breast
Fibroblasts
hESCs
Prostrate
Eye
Airway
Pancreas
Stomach
Multipotent cells
0
2500
5000
7500
Number of samples
Source
GTEx
Only in Recount3

Figure 2

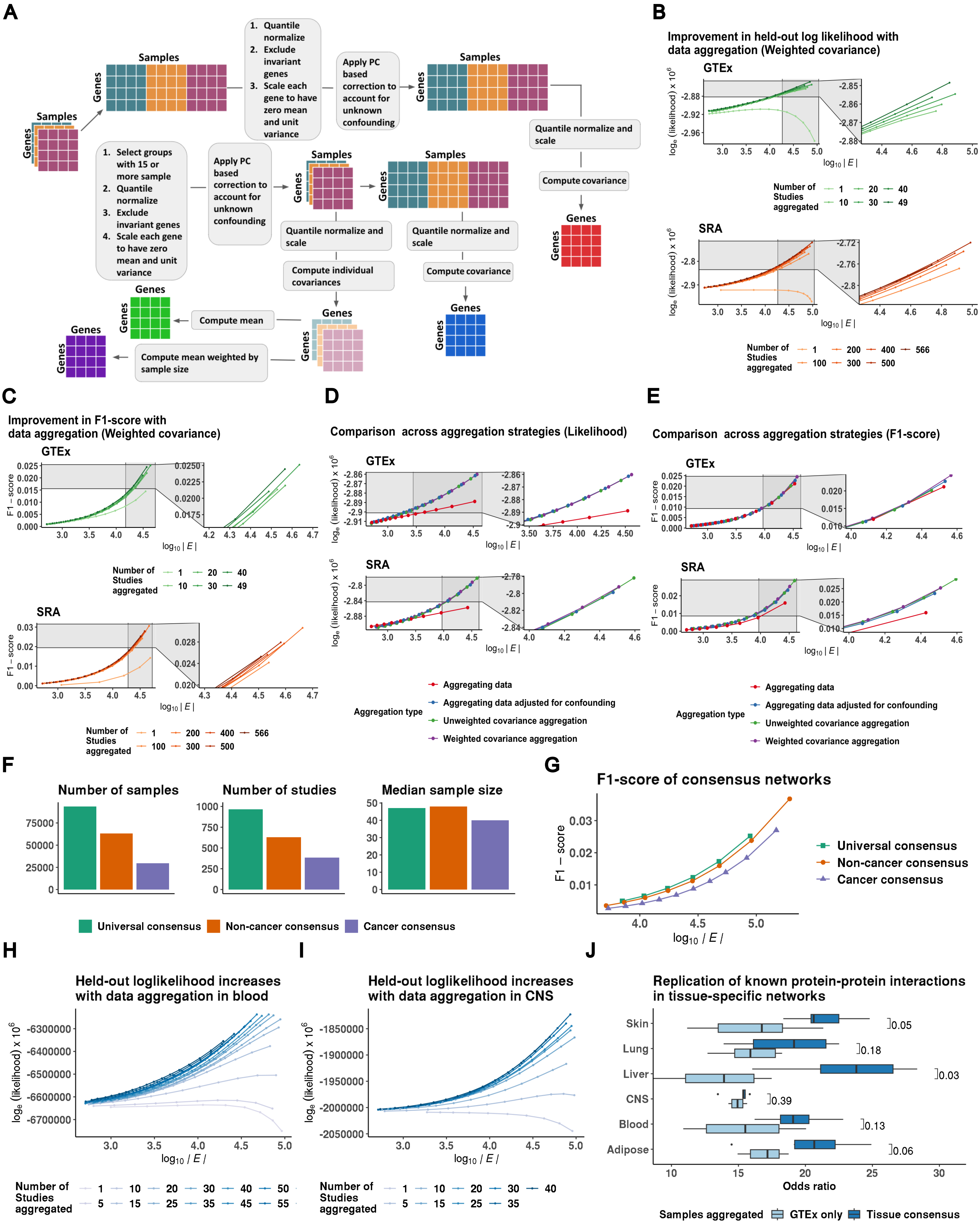
A
Samples
Genes
1. Quantile normalize
2. Exclude invariant genes
3. Scale each gene to have zero mean and unit variance
Apply PC based correction to account for unknown confounding
Quantile normalize and scale
Compute covariance
1. Select groups with 15 or more sample
2. Quantile normalize
3. Exclude invariant genes
4. Scale each gene to have zero mean and unit variance
Compute individual covariances
Compute mean
Compute mean weighted by sample size
B
Improvement in held-out log likelihood with data aggregation (Weighted covariance)
GTEx
SRA
log$_e$ (likelihood) x 10^6
log$_{10}$ | E |
Number of Studies aggregated
1, 10, 20, 30, 40, 49
1, 100, 200, 300, 400, 500, 566
C
Improvement in F1-score with data aggregation (Weighted covariance)
GTEx
SRA
F1 – score
log$_{10}$ | E |
Number of Studies aggregated
D
Comparison across aggregation strategies (Likelihood)
E
Comparison across aggregation strategies (F1-score)
Aggregation type
Aggregating data
Aggregating data adjusted for confounding
Unweighted covariance aggregation
Weighted covariance aggregation
F
Number of samples
Number of studies
Median sample size
Universal consensus
Non-cancer consensus
Cancer consensus
G
F1-score of consensus networks
F1 – score
log$_{10}$ / E /
H
Held-out loglikelihood increases with data aggregation in blood
-6300000
-6400000
-6500000
-6600000
-6700000
Number of Studies aggregated
1, 5, 10, 15, 20, 25, 30, 35, 40, 45, 50, 55
I
Held-out loglikelihood increases with data aggregation in CNS
-1850000
-1900000
-1950000
-2000000
-2050000
Number of Studies aggregated
1, 5, 10, 15, 20, 25, 30, 35, 40
J
Replication of known protein-protein interactions in tissue-specific networks
Skin 0.05
Lung 0.18
Liver 0.03
CNS 0.39
Blood 0.13
Adipose 0.06
Odds ratio
10, 15, 20, 25, 30
Samples aggregated
GTEx only
Tissue consensus

Figure 3

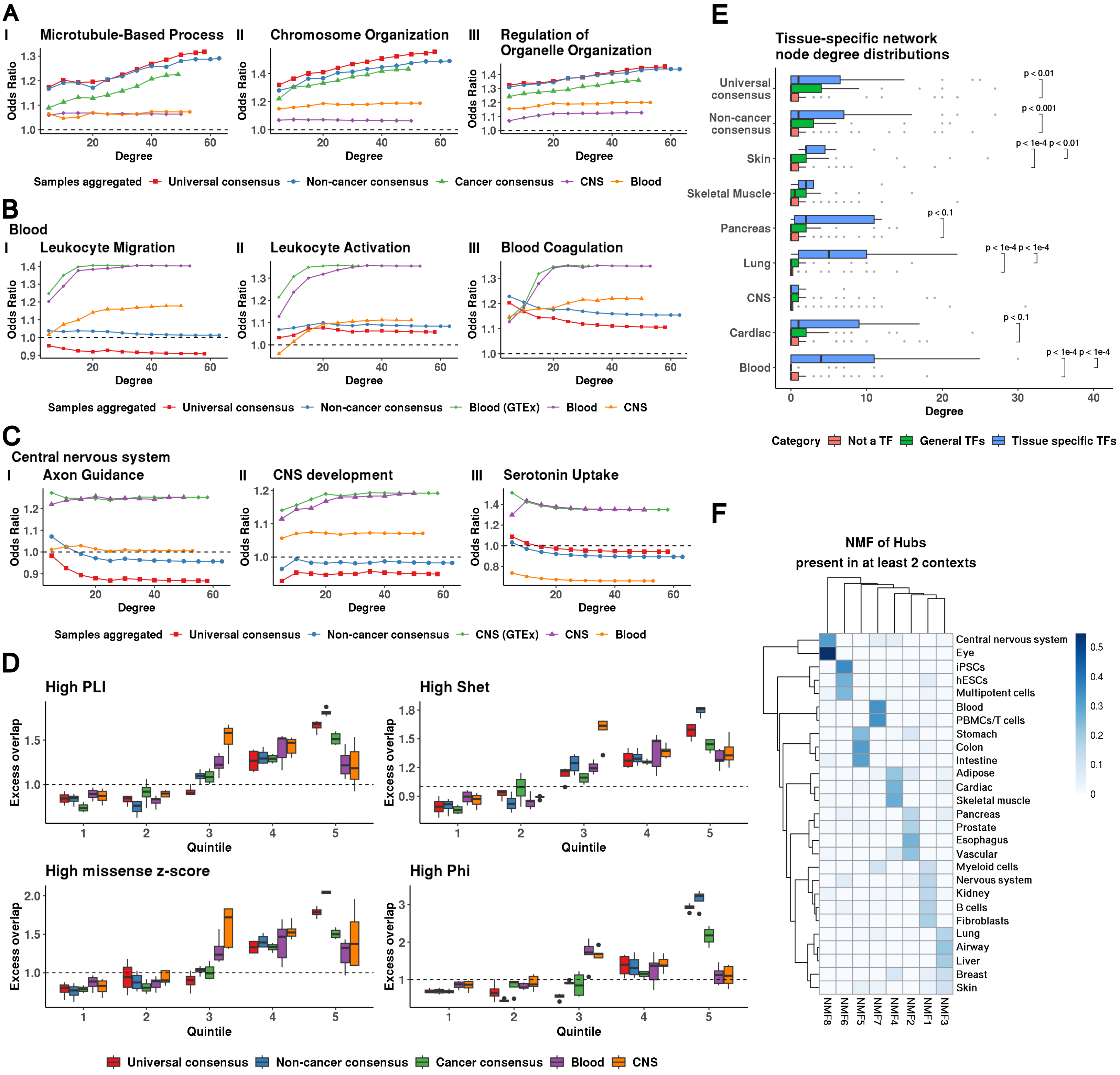
A
I Microtubule-Based Process
II Chromosome Organization
III Regulation of Organelle Organization
Odds Ratio
Degree
Samples aggregated
Universal consensus
Non-cancer consensus
Cancer consensus
CNS
Blood
B
Blood
I Leukocyte Migration
II Leukocyte Activation
III Blood Coagulation
Odds Ratio
Degree
Samples aggregated
Universal consensus
Non-cancer consensus
Blood (GTEx)
Blood
CNS
C
Central nervous system
I Axon Guidance
II CNS development
III Serotonin Uptake
Odds Ratio
Degree
Samples aggregated
Universal consensus
Non-cancer consensus
CNS (GTEx)
CNS
Blood
D
High PLI
High Shet
High missense z-score
High Phi
Excess overlap
Quintile
Universal consensus
Non-cancer consensus
Cancer consensus
Blood
CNS
E
Tissue-specific network node degree distributions
Universal consensus
Non-cancer consensus
Skin
Skeletal Muscle
Pancreas
Lung
CNS
Cardiac
Blood
p < 0.01
p < 0.001
p < 1e-4
p < 0.01
p < 0.1
p < 1e-4
p < 1e-4
p < 0.1
p < 1e-4
p < 1e-4
Degree
Category
Not a TF
General TFs
Tissue specific TFs
F
NMF of Hubs present in at least 2 contexts
Central nervous system
Eye
iPSCs
hESCs
Multipotent cells
Blood
PBMCs/T cells
Stomach
Colon
Intestine
Adipose
Cardiac
Skeletal muscle
Pancreas
Prostate
Esophagus
Vascular
Myeloid cells
Nervous system
Kidney
B cells
Fibroblasts
Lung
Airway
Liver
Breast
Skin
NMF8
NMF6
NMF5
NMF7
NMF4
NMF2
NMF1
NMF3
0.5
0.4
0.3
0.2
0.1
0

Figure 4

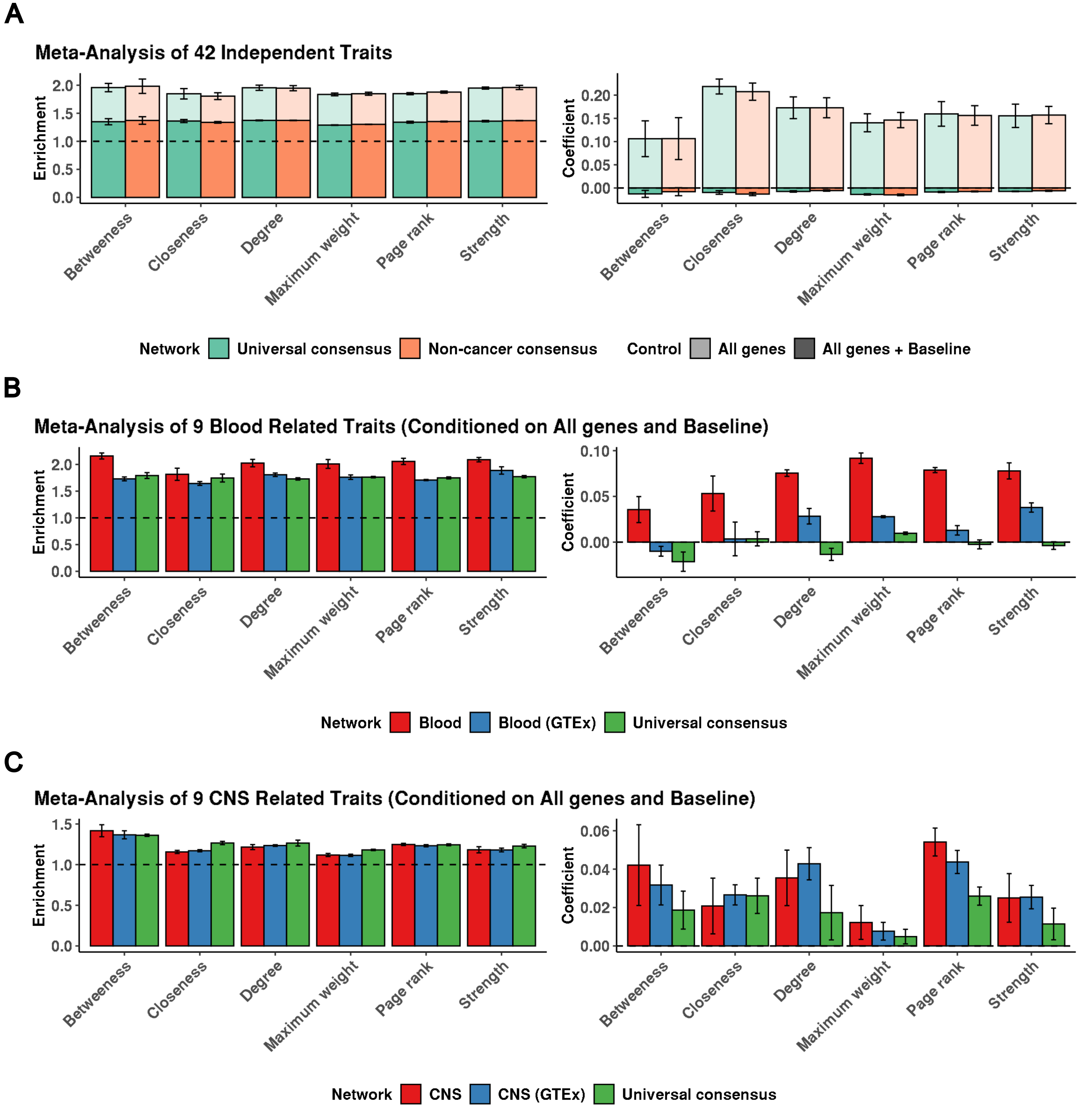
A
Meta-Analysis of 42 Independent Traits
Enrichment
2.0
1.5
1.0
0.5
0.0
Coefficient
0.20
0.15
0.10
0.05
0.00
Betweeness
Closeness
Degree
Maximum weight
Page rank
Strength
Network
Universal consensus
Non-cancer consensus
Control
All genes
All genes + Baseline
B
Meta-Analysis of 9 Blood Related Traits (Conditioned on All genes and Baseline)
Enrichment
2.0
1.5
1.0
0.5
0.0
Coefficient
0.10
0.05
0.00
Betweeness
Closeness
Degree
Maximum weight
Page rank
Strength
Network
Blood
Blood (GTEx)
Universal consensus
C
Meta-Analysis of 9 CNS Related Traits (Conditioned on All genes and Baseline)
Enrichment
1.5
1.0
0.5
0.0
Coefficient
0.06
0.04
0.02
0.00
Betweeness
Closeness
Degree
Maximum weight
Page rank
Strength
Network
CNS
CNS (GTEx)
Universal consensus